FERMILAB-PUB-04-440-E
Submitted to PRD, December 23, 2004

Measurement of the J/ψ Meson and b-Hadron Production Cross Sections in $p\bar{p}$ Collisions at $\sqrt{s} = 1960\,\mathrm{GeV}$

D. Acosta,[16] J. Adelman,[12] T. Affolder,[9] T. Akimoto,[54] M.G. Albrow,[15] D. Ambrose,[43] S. Amerio,[42] D. Amidei,[33] A. Anastassov,[50] K. Anikeev,[15] A. Annovi,[44] J. Antos,[1] M. Aoki,[54] G. Apollinari,[15] T. Arisawa,[56] J-F. Arguin,[32] A. Artikov,[13] W. Ashmanskas,[15] A. Attal,[7] F. Azfar,[41] P. Azzi-Bacchetta,[42] N. Bacchetta,[42] H. Bachacou,[28] W. Badgett,[15] A. Barbaro-Galtieri,[28] G.J. Barker,[25] V.E. Barnes,[46] B.A. Barnett,[24] S. Baroiant,[6] M. Barone,[17] G. Bauer,[31] F. Bedeschi,[44] S. Behari,[24] S. Belforte,[53] G. Bellettini,[44] J. Bellinger,[58] E. Ben-Haim,[15] D. Benjamin,[14] A. Beretvas,[15] A. Bhatti,[48] M. Binkley,[15] D. Bisello,[42] M. Bishai,[15] R.E. Blair,[2] C. Blocker,[5] K. Bloom,[33] B. Blumenfeld,[24] A. Bocci,[48] A. Bodek,[47] G. Bolla,[46] A. Bolshov,[31] P.S.L. Booth,[29] D. Bortoletto,[46] J. Boudreau,[45] S. Bourov,[15] B. Brau,[9] C. Bromberg,[34] E. Brubaker,[12] J. Budagov,[13] H.S. Budd,[47] K. Burkett,[15] G. Busetto,[42] P. Bussey,[19] K.L. Byrum,[2] S. Cabrera,[14] M. Campanelli,[18] M. Campbell,[33] A. Canepa,[46] M. Casarsa,[53] D. Carlsmith,[58] S. Carron,[14] R. Carosi,[44] M. Cavalli-Sforza,[3] A. Castro,[4] P. Catastini,[44] D. Cauz,[53] A. Cerri,[28] L. Cerrito,[23] J. Chapman,[33] C. Chen,[43] Y.C. Chen,[1] M. Chertok,[6] G. Chiarelli,[44] G. Chlachidze,[13] F. Chlebana,[15] I. Cho,[27] K. Cho,[27] D. Chokheli,[13] J.P. Chou,[20] M.L. Chu,[1] S. Chuang,[58] J.Y. Chung,[38] W-H. Chung,[58] Y.S. Chung,[47] C.I. Ciobanu,[23] M.A. Ciocci,[44] A.G. Clark,[18] D. Clark,[5] M. Coca,[47] A. Connolly,[28] M. Convery,[48] J. Conway,[6] B. Cooper,[30] M. Cordelli,[17] G. Cortiana,[42] J. Cranshaw,[52] J. Cuevas,[10] R. Culbertson,[15] C. Currat,[28] D. Cyr,[58] D. Dagenhart,[5] S. Da Ronco,[42] S. D'Auria,[19] P. de Barbaro,[47] S. De Cecco,[49] G. De Lentdecker,[47] S. Dell'Agnello,[17] M. Dell'Orso,[44] S. Demers,[47] L. Demortier,[48] M. Deninno,[4] D. De Pedis,[49] P.F. Derwent,[15] C. Dionisi,[49] J.R. Dittmann,[15] C. Dörr,[25] P. Doksus,[23] A. Dominguez,[28] S. Donati,[44] M. Donega,[18] J. Donini,[42] M. D'Onofrio,[18] T. Dorigo,[42] V. Drollinger,[36] K. Ebina,[56] N. Eddy,[23] J. Ehlers,[18] R. Ely,[28] R. Erbacher,[6] M. Erdmann,[25] D. Errede,[23] S. Errede,[23] R. Eusebi,[47] H-C. Fang,[28] S. Farrington,[29] I. Fedorko,[44] W.T. Fedorko,[12] R.G. Feild,[59] M. Feindt,[25] J.P. Fernandez,[46] C. Ferretti,[33] R.D. Field,[16] G. Flanagan,[34] B. Flaugher,[15] L.R. Flores-Castillo,[45] A. Foland,[20] S. Forrester,[6] G.W. Foster,[15] M. Franklin,[20] J.C. Freeman,[28] Y. Fujii,[26] I. Furic,[12] A. Gajjar,[29] A. Gallas,[37] J. Galyardt,[11] M. Gallinaro,[48] M. Garcia-Sciveres,[28]

A.F. Garfinkel,[46] C. Gay,[59] H. Gerberich,[14] D.W. Gerdes,[33] E. Gerchtein,[11]
S. Giagu,[49] P. Giannetti,[44] A. Gibson,[28] K. Gibson,[11] C. Ginsburg,[58] K. Giolo,[46]
M. Giordani,[53] M. Giunta,[44] G. Giurgiu,[11] V. Glagolev,[13] D. Glenzinski,[15] M. Gold,[36]
N. Goldschmidt,[33] D. Goldstein,[7] J. Goldstein,[41] G. Gomez,[10] G. Gomez-Ceballos,[10]
M. Goncharov,[51] O. González,[46] I. Gorelov,[36] A.T. Goshaw,[14] Y. Gotra,[45] K. Goulianos,[48]
A. Gresele,[4] M. Griffiths,[29] C. Grosso-Pilcher,[12] U. Grundler,[23] M. Guenther,[46]
J. Guimaraes da Costa,[20] C. Haber,[28] K. Hahn,[43] S.R. Hahn,[15] E. Halkiadakis,[47]
A. Hamilton,[32] B-Y. Han,[47] R. Handler,[58] F. Happacher,[17] K. Hara,[54] M. Hare,[55]
R.F. Harr,[57] R.M. Harris,[15] F. Hartmann,[25] K. Hatakeyama,[48] J. Hauser,[7] C. Hays,[14]
H. Hayward,[29] E. Heider,[55] B. Heinemann,[29] J. Heinrich,[43] M. Hennecke,[25] M. Herndon,[24]
C. Hill,[9] D. Hirschbuehl,[25] A. Hocker,[47] K.D. Hoffman,[12] A. Holloway,[20] S. Hou,[1]
M.A. Houlden,[29] B.T. Huffman,[41] Y. Huang,[14] R.E. Hughes,[38] J. Huston,[34] K. Ikado,[56]
J. Incandela,[9] G. Introzzi,[44] M. Iori,[49] Y. Ishizawa,[54] C. Issever,[9] A. Ivanov,[47] Y. Iwata,[22]
B. Iyutin,[31] E. James,[15] D. Jang,[50] J. Jarrell,[36] D. Jeans,[49] H. Jensen,[15] E.J. Jeon,[27]
M. Jones,[46] K.K. Joo,[27] S.Y. Jun,[11] T. Junk,[23] T. Kamon,[51] J. Kang,[33] M. Karagoz Unel,[37]
P.E. Karchin,[57] S. Kartal,[15] Y. Kato,[40] Y. Kemp,[25] R. Kephart,[15] U. Kerzel,[25]
V. Khotilovich,[51] B. Kilminster,[38] D.H. Kim,[27] H.S. Kim,[23] J.E. Kim,[27] M.J. Kim,[11]
M.S. Kim,[27] S.B. Kim,[27] S.H. Kim,[54] T.H. Kim,[31] Y.K. Kim,[12] B.T. King,[29] M. Kirby,[14]
L. Kirsch,[5] S. Klimenko,[16] B. Knuteson,[31] B.R. Ko,[14] H. Kobayashi,[54] P. Koehn,[38]
D.J. Kong,[27] K. Kondo,[56] J. Konigsberg,[16] K. Kordas,[32] A. Korn,[31] A. Korytov,[16]
K. Kotelnikov,[35] A.V. Kotwal,[14] A. Kovalev,[43] J. Kraus,[23] I. Kravchenko,[31] A. Kreymer,[15]
J. Kroll,[43] M. Kruse,[14] V. Krutelyov,[51] S.E. Kuhlmann,[2] S. Kwang,[12] A.T. Laasanen,[46]
S. Lai,[32] S. Lami,[48] S. Lammel,[15] J. Lancaster,[14] M. Lancaster,[30] R. Lander,[6] K. Lannon,[38]
A. Lath,[50] G. Latino,[36] R. Lauhakangas,[21] I. Lazzizzera,[42] Y. Le,[24] C. Lecci,[25]
T. LeCompte,[2] J. Lee,[27] J. Lee,[47] S.W. Lee,[51] R. Lefèvre,[3] N. Leonardo,[31] S. Leone,[44]
S. Levy,[12] J.D. Lewis,[15] K. Li,[59] C. Lin,[59] C.S. Lin,[15] M. Lindgren,[15] T.M. Liss,[23]
A. Lister,[18] D.O. Litvintsev,[15] T. Liu,[15] Y. Liu,[18] N.S. Lockyer,[43] A. Loginov,[35] M. Loreti,[42]
P. Loverre,[49] R-S. Lu,[1] D. Lucchesi,[42] P. Lujan,[28] P. Lukens,[15] G. Lungu,[16] L. Lyons,[41]
J. Lys,[28] R. Lysak,[1] D. MacQueen,[32] R. Madrak,[15] K. Maeshima,[15] P. Maksimovic,[24]
L. Malferrari,[4] G. Manca,[29] R. Marginean,[38] C. Marino,[23] A. Martin,[24] M. Martin,[59]

V. Martin,[37] M. Martínez,[3] T. Maruyama,[54] H. Matsunaga,[54] M. Mattson,[57] P. Mazzanti,[4]
K.S. McFarland,[47] D. McGivern,[30] P.M. McIntyre,[51] P. McNamara,[50] R. NcNulty,[29]
A. Mehta,[29] S. Menzemer,[31] A. Menzione,[44] P. Merkel,[15] C. Mesropian,[48] A. Messina,[49]
T. Miao,[15] N. Miladinovic,[5] L. Miller,[20] R. Miller,[34] J.S. Miller,[33] R. Miquel,[28] S. Miscetti,[17]
G. Mitselmakher,[16] A. Miyamoto,[26] Y. Miyazaki,[40] N. Moggi,[4] B. Mohr,[7] R. Moore,[15]
M. Morello,[44] P.A. Movilla Fernandez,[28] A. Mukherjee,[15] M. Mulhearn,[31] T. Muller,[25]
R. Mumford,[24] A. Munar,[43] P. Murat,[15] J. Nachtman,[15] S. Nahn,[59] I. Nakamura,[43]
I. Nakano,[39] A. Napier,[55] R. Napora,[24] D. Naumov,[36] V. Necula,[16] F. Niell,[33] J. Nielsen,[28]
C. Nelson,[15] T. Nelson,[15] C. Neu,[43] M.S. Neubauer,[8] C. Newman-Holmes,[15] T. Nigmanov,[45]
L. Nodulman,[2] O. Norniella,[3] K. Oesterberg,[21] T. Ogawa,[56] S.H. Oh,[14] Y.D. Oh,[27]
T. Ohsugi,[22] T. Okusawa,[40] R. Oldeman,[49] R. Orava,[21] W. Orejudos,[28] C. Pagliarone,[44]
E. Palencia,[10] R. Paoletti,[44] V. Papadimitriou,[15] S. Pashapour,[32] J. Patrick,[15]
G. Pauletta,[53] M. Paulini,[11] T. Pauly,[41] C. Paus,[31] D. Pellett,[6] A. Penzo,[53] T.J. Phillips,[14]
G. Piacentino,[44] J. Piedra,[10] K.T. Pitts,[23] C. Plager,[7] A. Pompoš,[46] L. Pondrom,[58]
G. Pope,[45] X. Portell,[3] O. Poukhov,[13] F. Prakoshyn,[13] T. Pratt,[29] A. Pronko,[16]
J. Proudfoot,[2] F. Ptohos,[17] G. Punzi,[44] J. Rademacker,[41] M.A. Rahaman,[45] A. Rakitine,[31]
S. Rappoccio,[20] F. Ratnikov,[50] H. Ray,[33] B. Reisert,[15] V. Rekovic,[36] P. Renton,[41]
M. Rescigno,[49] F. Rimondi,[4] K. Rinnert,[25] L. Ristori,[44] W.J. Robertson,[14] A. Robson,[41]
T. Rodrigo,[10] S. Rolli,[55] L. Rosenson,[31] R. Roser,[15] R. Rossin,[42] C. Rott,[46] J. Russ,[11]
V. Rusu,[12] A. Ruiz,[10] D. Ryan,[55] H. Saarikko,[21] S. Sabik,[32] A. Safonov,[6] R. St. Denis,[19]
W.K. Sakumoto,[47] G. Salamanna,[49] D. Saltzberg,[7] C. Sanchez,[3] A. Sansoni,[17]
L. Santi,[53] S. Sarkar,[49] K. Sato,[54] P. Savard,[32] A. Savoy-Navarro,[15] P. Schlabach,[15]
E.E. Schmidt,[15] M.P. Schmidt,[59] M. Schmitt,[37] L. Scodellaro,[10] A. Scribano,[44] F. Scuri,[44]
A. Sedov,[46] S. Seidel,[36] Y. Seiya,[40] F. Semeria,[4] L. Sexton-Kennedy,[15] I. Sfiligoi,[17]
M.D. Shapiro,[28] T. Shears,[29] P.F. Shepard,[45] D. Sherman,[20] M. Shimojima,[54]
M. Shochet,[12] Y. Shon,[58] I. Shreyber,[35] A. Sidoti,[44] J. Siegrist,[28] M. Siket,[1] A. Sill,[52]
P. Sinervo,[32] A. Sisakyan,[13] A. Skiba,[25] A.J. Slaughter,[15] K. Sliwa,[55] D. Smirnov,[36]
J.R. Smith,[6] F.D. Snider,[15] R. Snihur,[32] A. Soha,[6] S.V. Somalwar,[50] J. Spalding,[15]
M. Spezziga,[52] L. Spiegel,[15] F. Spinella,[44] M. Spiropulu,[9] P. Squillacioti,[44] H. Stadie,[25]
B. Stelzer,[32] O. Stelzer-Chilton,[32] J. Strologas,[36] D. Stuart,[9] A. Sukhanov,[16] K. Sumorok,[31]

H. Sun,[55] T. Suzuki,[54] A. Taffard,[23] R. Tafirout,[32] S.F. Takach,[57] H. Takano,[54] R. Takashima,[22] Y. Takeuchi,[54] K. Takikawa,[54] M. Tanaka,[2] R. Tanaka,[39] N. Tanimoto,[39] S. Tapprogge,[21] M. Tecchio,[33] P.K. Teng,[1] K. Terashi,[48] R.J. Tesarek,[15] S. Tether,[31] J. Thom,[15] A.S. Thompson,[19] E. Thomson,[43] P. Tipton,[47] V. Tiwari,[11] S. Tkaczyk,[15] D. Toback,[51] K. Tollefson,[34] T. Tomura,[54] D. Tonelli,[44] M. Tönnesmann,[34] S. Torre,[44] D. Torretta,[15] S. Tourneur,[15] W. Trischuk,[32] J. Tseng,[41] R. Tsuchiya,[56] S. Tsuno,[39] D. Tsybychev,[16] N. Turini,[44] M. Turner,[29] F. Ukegawa,[54] T. Unverhau,[19] S. Uozumi,[54] D. Usynin,[43] L. Vacavant,[28] A. Vaiciulis,[47] A. Varganov,[33] E. Vataga,[44] S. Vejcik III,[15] G. Velev,[15] V. Veszpremi,[46] G. Veramendi,[23] T. Vickey,[23] R. Vidal,[15] I. Vila,[10] R. Vilar,[10] I. Vollrath,[32] I. Volobouev,[28] M. von der Mey,[7] P. Wagner,[51] R.G. Wagner,[2] R.L. Wagner,[15] W. Wagner,[25] R. Wallny,[7] T. Walter,[25] T. Yamashita,[39] K. Yamamoto,[40] Z. Wan,[50] M.J. Wang,[1] S.M. Wang,[16] A. Warburton,[32] B. Ward,[19] S. Waschke,[19] D. Waters,[30] T. Watts,[50] M. Weber,[28] W.C. Wester III,[15] B. Whitehouse,[55] A.B. Wicklund,[2] E. Wicklund,[15] H.H. Williams,[43] P. Wilson,[15] B.L. Winer,[38] P. Wittich,[43] S. Wolbers,[15] C. Wolfe,[12] M. Wolter,[55] M. Worcester,[7] S. Worm,[50] T. Wright,[33] X. Wu,[18] F. Würthwein,[8] A. Wyatt,[30] A. Yagil,[15] C. Yang,[59] U.K. Yang,[12] W. Yao,[28] G.P. Yeh,[15] K. Yi,[24] J. Yoh,[15] P. Yoon,[47] K. Yorita,[56] T. Yoshida,[40] I. Yu,[27] S. Yu,[43] Z. Yu,[59] J.C. Yun,[15] L. Zanello,[49] A. Zanetti,[53] I. Zaw,[20] F. Zetti,[44] J. Zhou,[50] A. Zsenei,[18] and S. Zucchelli,[4]

(CDF Collaboration)

[1] *Institute of Physics, Academia Sinica, Taipei, Taiwan 11529, Republic of China*

[2] *Argonne National Laboratory, Argonne, Illinois 60439*

[3] *Institut de Fisica d'Altes Energies, Universitat Autonoma de Barcelona, E-08193, Bellaterra (Barcelona), Spain*

[4] *Istituto Nazionale di Fisica Nucleare, University of Bologna, I-40127 Bologna, Italy*

[5] *Brandeis University, Waltham, Massachusetts 02254*

[6] *University of California at Davis, Davis, California 95616*

[7] *University of California at Los Angeles, Los Angeles, California 90024*

[8] *University of California at San Diego, La Jolla, California 92093*

[9] *University of California at Santa Barbara, Santa Barbara, California 93106*

[10] Instituto de Fisica de Cantabria, CSIC-University of Cantabria, 39005 Santander, Spain

[11] Carnegie Mellon University, Pittsburgh, PA 15213

[12] Enrico Fermi Institute, University of Chicago, Chicago, Illinois 60637

[13] Joint Institute for Nuclear Research, RU-141980 Dubna, Russia

[14] Duke University, Durham, North Carolina 27708

[15] Fermi National Accelerator Laboratory, Batavia, Illinois 60510

[16] University of Florida, Gainesville, Florida 32611

[17] Laboratori Nazionali di Frascati, Istituto Nazionale di Fisica Nucleare, I-00044 Frascati, Italy

[18] University of Geneva, CH-1211 Geneva 4, Switzerland

[19] Glasgow University, Glasgow G12 8QQ, United Kingdom

[20] Harvard University, Cambridge, Massachusetts 02138

[21] The Helsinki Group: Helsinki Institute of Physics; and Division of High Energy Physics, Department of Physical Sciences, University of Helsinki, FIN-00044, Helsinki, Finland

[22] Hiroshima University, Higashi-Hiroshima 724, Japan

[23] University of Illinois, Urbana, Illinois 61801

[24] The Johns Hopkins University, Baltimore, Maryland 21218

[25] Institut für Experimentelle Kernphysik, Universität Karlsruhe, 76128 Karlsruhe, Germany

[26] High Energy Accelerator Research Organization (KEK), Tsukuba, Ibaraki 305, Japan

[27] Center for High Energy Physics: Kyungpook National University, Taegu 702-701; Seoul National University, Seoul 151-742; and SungKyunKwan University, Suwon 440-746; Korea

[28] Ernest Orlando Lawrence Berkeley National Laboratory, Berkeley, California 94720

[29] University of Liverpool, Liverpool L69 7ZE, United Kingdom

[30] University College London, London WC1E 6BT, United Kingdom

[31] Massachusetts Institute of Technology, Cambridge, Massachusetts 02139

[32] Institute of Particle Physics: McGill University, Montréal, Canada H3A 2T8; and University of Toronto, Toronto, Canada M5S 1A7

[33] University of Michigan, Ann Arbor, Michigan 48109

[34] Michigan State University, East Lansing, Michigan 48824

[35] Institution for Theoretical and Experimental Physics, ITEP, Moscow 117259, Russia

[36] University of New Mexico, Albuquerque, New Mexico 87131

[37] Northwestern University, Evanston, Illinois 60208

[38] The Ohio State University, Columbus, Ohio 43210

[39] Okayama University, Okayama 700-8530, Japan

[40] Osaka City University, Osaka 588, Japan

[41] University of Oxford, Oxford OX1 3RH, United Kingdom

[42] University of Padova, Istituto Nazionale di Fisica Nucleare, Sezione di Padova-Trento, I-35131 Padova, Italy

[43] University of Pennsylvania, Philadelphia, Pennsylvania 19104

[44] Istituto Nazionale di Fisica Nucleare, University and Scuola Normale Superiore of Pisa, I-56100 Pisa, Italy

[45] University of Pittsburgh, Pittsburgh, Pennsylvania 15260

[46] Purdue University, West Lafayette, Indiana 47907

[47] University of Rochester, Rochester, New York 14627

[48] The Rockefeller University, New York, New York 10021

[49] Istituto Nazionale di Fisica Nucleare, Sezione di Roma 1, University di Roma "La Sapienza," I-00185 Roma, Italy

[50] Rutgers University, Piscataway, New Jersey 08855

[51] Texas A&M University, College Station, Texas 77843

[52] Texas Tech University, Lubbock, Texas 79409

[53] Istituto Nazionale di Fisica Nucleare, University of Trieste/ Udine, Italy

[54] University of Tsukuba, Tsukuba, Ibaraki 305, Japan

[55] Tufts University, Medford, Massachusetts 02155

[56] Waseda University, Tokyo 169, Japan

[57] Wayne State University, Detroit, Michigan 48201

[58] University of Wisconsin, Madison, Wisconsin 53706

[59] Yale University, New Haven, Connecticut 06520

Abstract

We present a new measurement of the inclusive and differential production cross sections of J/ψ mesons and b-hadrons in proton-antiproton collisions at $\sqrt{s} = 1960\,\mathrm{GeV}$. The data correspond to an integrated luminosity of 39.7 pb^{-1} collected by the CDF Run II detector. We find the integrated cross section for inclusive J/ψ production for all transverse momenta from 0 to $20\,\mathrm{GeV}/c$ in the rapidity range $|y| < 0.6$ to be $4.08 \pm 0.02(stat)^{+0.36}_{-0.33}(syst)$ μb. We separate the fraction of J/ψ events from the decay of the long-lived b-hadrons using the lifetime distribution in all events with $p_T(J/\psi) > 1.25\,\mathrm{GeV}/c$. We find the total cross section for b-hadrons, including both hadrons and anti-hadrons, decaying to J/ψ with transverse momenta greater than $1.25\,\mathrm{GeV}/c$ in the rapidity range $|y(J/\psi)| < 0.6$, is $0.330 \pm 0.005(stat)^{+0.036}_{-0.033}(syst)$ μb. Using a Monte Carlo simulation of the decay kinematics of b-hadrons to all final states containing a J/ψ, we extract the first measurement of the total single b-hadron cross section down to zero transverse momentum at $\sqrt{s} = 1960\,\mathrm{GeV}$. We find the total single b-hadron cross section integrated over all transverse momenta for b-hadrons in the rapidity range $|y| < 0.6$ to be $17.6 \pm 0.4(stat)^{+2.5}_{-2.3}(syst)$ μb.

PACS numbers: 13.85.Qk, 13.20.Gd, 14.40.Gx, 12.38.Qk

I. INTRODUCTION

The production of both charmonium mesons and bottom-flavored hadrons (referred to as b-hadrons or H_b in this paper) in proton-antiproton colliders has sustained continued interest over the last several years. There are three major sources of the J/ψ mesons: directly produced J/ψ, prompt decays of heavier charmonium states such as ${}^3P_1$ state χ_{c1} and ${}^3P_2$ state χ_{c2}, and decays of b-hadrons. Early hadroproduction models of quarkonium states could not describe the cross section of directly produced J/ψ mesons. These models under-predicted the measurements by a factor of approximately 50, and did not adequately describe the cross-section shape [1]. With the advent of the effective field theory, nonrelativistic QCD (NRQCD) [2], better theoretical descriptions of quarkonium production became possible. Within the NRQCD factorization formalism, the color-octet model provides a means to bring theory into better agreement with data [3, 4]. The fundamental idea of this model is that while a $(c\bar{c})$ meson has to be in a color-singlet state, the initially produced quark-antiquark pair does not. One can produce, for example, a $(c\bar{c})$ pair in a color-octet ${}^3P$ state which can then produce a color singlet ${}^3S_1$ J/ψ meson by single-gluon emission. This is done at the cost of adding a small number of parameters to the theory that currently must be determined by experiment. While the color-octet model can accommodate a large cross section, strictly speaking it does not predict it. There are other deficiencies of the NRQCD formalism; for example, NRQCD expects the spin alignment to be predominantly in the transverse state for the prompt J/ψ mesons with large transverse momenta, a prediction that is not in agreement with subsequent measurement [5].

Previous prompt, direct, and inclusive J/ψ cross-section measurements [1] from CDF required a minimum transverse momentum of $5\,\mathrm{GeV}/c$ on the J/ψ although greater than 90% of the cross section has been expected to lie below this point. In this paper we present the first measurement of the inclusive central J/ψ cross section over a much larger range of transverse momenta from zero to $20\,\mathrm{GeV}/c$. The J/ψ mesons are reconstructed from the decay channel $J/\psi \to \mu^+\mu^-$. The measurement was made possible by improving the CDF di-muon trigger capability to be sensitive to J/ψ with zero transverse momenta.

A significant fraction of J/ψ mesons produced at the Tevatron come from the decays of b-hadrons. In this experiment, we use the large sample of $H_b \to J/\psi X$ events to measure the inclusive b-hadron cross section. The previous Tevatron measurements [6–12] of the

b-hadron cross section in proton-antiproton collisions at $\sqrt{s} = 1800\,\mathrm{GeV}$ were substantially larger (by a factor of two to three) than that predicted by next-to-leading order (NLO) QCD calculations [13–15]. This was particularly puzzling since the UA1 measurements at $\sqrt{s} = 630\,\mathrm{GeV}$ [16] did not show such a marked departure from the NLO QCD calculations. Several theoretical explanations were suggested: higher-order corrections are large, intrinsic k_T effects are large [17], extreme values of the renormalization scales are needed, or new methods of resummation and fragmentation are required [18–20]. Theories of new and exotic sources of b-hadrons have also been proposed [21]. Since the earlier Tevatron results covered only 10-13% of the inclusive p_T spectrum, it was not evident whether the excess was due to an overall increase in the b-hadron production rate or a shift in the spectrum toward higher p_T.

An inclusive measurement of b-hadron production over all transverse momenta can help resolve this problem. Bottom hadrons have long lifetimes, on the order of picoseconds [22], which correspond to flight distances of several hundred microns at CDF. We use the measured distance between the J/ψ decay point and the beamline to separate prompt production of charmonium from b-hadron decays. The single b-hadron cross section is then extracted from the measurement of the cross section of J/ψ mesons from long-lived b-hadrons where single differentiates the cross section from the b-hadron cross section referring to b and $\bar{b}$ hadrons which is a factor of two bigger. In this paper, we present the first measurement of the inclusive single b-hadron cross section at $\sqrt{s} = 1960\,\mathrm{GeV}$ measured over all transverse momenta in the rapidity range $|y| < 0.6$.

II. DESCRIPTION OF THE EXPERIMENT

A. The Tevatron

The Fermilab Tevatron is a 1 km radius superconducting synchrotron. Thirty-six bunches of 980 GeV protons and antiprotons counter-circulate in a single ring and collide at two interaction points (where the CDF and D0 detectors are located) every 396 ns. The transverse profile of the interaction region can be approximately described by a circular Gaussian distribution with a typical RMS width of 30 μm. The longitudinal profile is also approximately Gaussian with a typical RMS of 30 cm.

For the data used in this analysis, instantaneous luminosities were in the range 0.5 to 2.0×10^{31} cm^{-2}s^{-1}. At these luminosities, typically there was only a single collision in a triggered event.

B. The CDF Detector

In the CDF detector [23, 24], a silicon vertex detector (SVX II) [25], located immediately outside the beam pipe, provides precise three-dimensional track reconstruction and is used to identify displaced vertices associated with b and c hadron decays. The momentum of charged particles is measured precisely in the central outer tracker (COT) [26], a multi-wire drift chamber that sits inside a 1.4 T superconducting solenoidal magnet. Outside the COT are electromagnetic and hadronic calorimeters arranged in a projective-tower geometry, covering the pseudo-rapidity region $|\eta| < 3.5$. Drift chambers and scintillator counters in the region $|\eta| < 1.5$ provide muon identification outside the calorimeters. In the CDF coordinate system, θ and ϕ are the polar and azimuthal angles, respectively, defined with respect to the proton beam direction, z. The pseudorapidity η is defined as $-\ln\tan(\theta/2)$. The transverse momentum of a particle is $p_T = p\sin(\theta)$.

The portion of the silicon detector systems used in this analysis is the SVX II detector. The SVX II consists of double-sided micro-strip sensors arranged in five concentric cylindrical shells with radii between 2.5 and 10.6 cm. The detector is divided into 3 contiguous five-layer sections along the beam direction for a total z coverage of 90 cm. Each barrel is divided into twelve azimuthal wedges of 30° each. Each of the five layers in a wedge is further divided into two electrically independent modules called ladders. There are a total of 360 ladders in the SVX II detector. The fraction of functioning ladders was increasing from 78% to 94% during the period between February 2002 and July 2002 in which the data used in this paper were taken while the SVX detector was being commissioned.

The COT is the main tracking chamber in CDF. It is a cylindrical drift chamber segmented into eight concentric superlayers filled with a mixture of 50% Argon and 50% Ethane. The active volume covers $|z| < 155$ cm and 40 to 140 cm in radius. Each superlayer is sectioned in ϕ into separate cells. A cell is defined as one sense plane with two adjacent grounded field sheets. The sense plane is composed of 40 μm gold-plated tungsten wires, twelve of which are sense wires. In the middle of the sense planes, a mechanical spacer made of polyester/fiber glass rod is epoxied to each wire to limit the stepping of wires out of the plane due to electrostatic forces. The main body of the field sheets is 10 μm gold-coated mylar. The field sheets approximate true grounded wire planes much better than the arrays of wires which have often been used in wire chambers including the predecessor to the COT. Use of the field sheet also results in a smaller amount of material within the tracking volume, and allows the COT to operate at a much higher drift field than is possible with an array of wires. The eight superlayers of the COT alternate between stereo and axial, beginning with superlayer 1, which is a stereo layer. In an axial layer, the wires and field sheets are parallel to the z axis, and thus provide only r-ϕ information. In stereo layers, the wires and field sheets are arranged with a stereo angle of $\pm 2^\circ$ and provide z information in addition to r-ϕ.

The CDF central muon detector (CMU) [27] is located around the outside of the central hadron calorimeter at a radius of 347 cm from the beam axis. The calorimeter is formed from 48 wedges, 24 on the east (positive z), and 24 on the west (negative z), each wedge covering 15° in ϕ. The calorimeter thickness is about 5.5 interaction lengths for hadron attenuation. The muon drift cells with seven wires parallel to the beamline are 226 cm long and cover 12.6° in ϕ. There is a 2.4° gap between drift cell arrays, giving a ϕ coverage of 84%. The pseudorapidity coverage relative to the center of the beam-beam interaction volume is $0.03 < |\eta| < 0.63$. Each wedge is further segmented azimuthally into three 4.2° modules. Each module consists of four layers of four rectangular drift cells. The sense wires in alternating layers are offset by 2 mm for ambiguity resolution. The smallest unit in the CMU, called a stack, covers about 1.2° and includes four drift cells, one from each layer. Adjacent pairs of stacks are combined together to form a two-stack unit called a tower. A track segment detected in these chambers is called a CMU stub.

A second set of muon drift chambers is located behind an additional 60 cm of steel (3.3 interaction lengths). The chambers are 640 cm long and are arranged axially to form a box around the central detector. This system is called the CMP, and muons which register a stub in both the CMU and the CMP are called CMUP muons.

Luminosity is measured using low-mass gaseous Cherenkov luminosity counters (CLC) [28, 29]. There are two CLC modules in the CDF detector installed at small angles in the proton and antiproton directions. Each module consists of 48 long, thin conical counters filled with isobutane gas and arranged in three concentric layers around the beam pipe.

C. Muon Reconstruction

The starting point for the selection of $J/\psi \to \mu^+\mu^-$ candidates is the reconstruction of two oppositely charged muons. Muons are reconstructed from tracks measured in the tracking chambers matched to the stub positions in the muon detectors.

1. *Charged Particle Tracking*

Track reconstruction begins in the COT. The first step in the pattern recognition is the formation of line segments from hits in each superlayer. Line segments from the axial layers that are tangent to a common circle are linked together to form a track candidate and the hit positions are fit to a circle. Line segments in stereo layers are then linked to the 2-dimensional track and a helix fit is performed. The transverse momentum resolution of the COT is measured using cosmic ray events to be

$$\frac{\sigma(p_T)}{p_T^2} = 0.0017\ [\mathrm{GeV}/c]^{-1}. \tag{1}$$

The next step is to extrapolate each COT track into the SVX II and add hits that are consistent with the track. A window around the track is established based on the errors on the COT track parameters. If a hit in the outer SVX II layer lies within the window, it is added to the track. A new track fit is then performed, resulting in a new error matrix and a new window. This window is then used to add hits from the next SVX II layer, and the procedure is repeated over all layers. If no hit is found within the search window, the algorithm proceeds to the next layer. There may be multiple track candidates with different combinations of SVX II hits associated with one COT track. In this case, the track with the largest number of SVX II layers with hits is chosen. A COT-SVX II track is formed only if at least three r-ϕ hits in the SVX II are associated with the original COT track. An averaged impact parameter resolution of 34 μm is achieved using hit information measured in SVX II for muon tracks with p_T around $1.5\,\mathrm{GeV}/c$.

2. *Muon Identification*

In the first stage of muon identification, hits in alternate layers that are within 7.5 cm of each other are used to form linear track segments. This distance corresponds to a maximum angle relative to the radial direction in the chamber of 65°. The remaining pair of layers is then searched for hits within 0.5 cm of the line segment. The procedure is iterated and the optimal set of hits is found. The segment resulting from a least-square fit to these hits is called a "stub". Hits are required in at least 3 of the 4 layers to form a stub.

Stubs reconstructed in the CMU are matched to tracks with a minimal p_T of 1.3 GeV/c. The tracks are extrapolated to the CMU after using a simplified geometry model to track the muon candidate's motion in the non-uniform magnetic field of the calorimeter. The distance, $\Delta r\phi$, in the r-ϕ plane between the track projected to the muon chambers and the muon stub is required to be less than 30 cm. The track is required to point to the same end of the CMU detector (east with postive z or west with negative z) that the stub is in unless the muon candidate track is within 20cm of the center of the detector.

D. Triggers

CDF uses a three-level trigger system [24]. At Level 1, data from every beam crossing is stored in a pipeline capable of buffering data from 42 beam-crossings. The Level 1 trigger either rejects the event or copies the data into one of four Level 2 buffers. During the data-taking period for this analysis, the global Level 1 accept rate was approximately 10 kHz corresponding to a rate reduction factor of approximately 170.

At Level 2, a substantial fraction of the event data is available for analysis by the trigger processors which require approximately 25 μs per event. During the period the data for this analysis were taken, the L2 accept rate was approximately 200 Hz, for a rejection factor of approximately 50.

Events that pass the Level 1 and Level 2 selection criteria are then sent to the Level 3 trigger [30], a cluster of computers running a speed-optimized reconstruction code. Events selected by Level 3 are written to permanent mass storage. During the period the data for this analysis were taken, the global Level 3 accept rate was approximately 40 Hz, for a rejection factor of approximately 5.

For the cross-section measurement, we require events with two muon candidates identified by the Level 1 trigger. In Level 1, track reconstruction is done by the eXtremely Fast Tracker (XFT) [31]. The XFT examines COT hits from the four axial superlayers and provides r-ϕ tracking information. The line segments are identified in each superlayer and linked using predetermined patterns. The XFT requires that each line segment contains hits found on at least ten of a possible twelve anode wires in each axial superlayer. The XFT finds tracks with $p_T > 1.5\,\mathrm{GeV}/c$. It subdivides the COT into azimuthal sections of $1.25°$ each and places a track into a given section based on its ϕ position at superlayer 6 ($r = 105.575\,\mathrm{cm}$). If more than one track candidate is found within a given section, the XFT return the track with the highest p_T. The XFT passes the tracks it finds to the eXTRaPolation unit (XTRP). The XTRP extrapolates an XFT track's trajectory to the CMU where a stub should be found if it is a muon, taking into account the path of the track in the magnetic field and the multiple scattering of muon in the calorimeter. The XTRP then passes the search window to the muon trigger crate, which looks for CMU stubs within the search window. A Level 1 CMU stub requires that there be hits on both even layers or both odd layers of one $1.05°$ stack of the CMU with a drift time difference Δt less than 396 ns. The twelve stacks in each $15°$ wedge of the CMU are mapped in pairs to six trigger towers to match the granularity of the XTRP extrapolation. If a muon stub is found within the search window, it is considered a Level 1 muon. In order to fire the di-muon trigger, two muon candidates must be found, separated by at least two CMU trigger towers. There is no requirement that the muons have opposite charge at Level 1. During the data taking period in which the di-muon sample used for this analysis was obtained, there was no additional selection imposed on muons at Level 2 and events were passed to Level 3 directly from Level 1.

At Level 3, the muons are required to have opposite charge, and to have an invariant mass between 2.7 and $4.0\,\mathrm{GeV}/c^2$. In addition, both muon tracks are required to be within 5 cm in z_0, where z_0 is the z coordinate of the muon track at its distance of the closest approach in the r-ϕ plane to the beam axis. For a portion of the data sample considered in this analysis, there is a requirement that the opening angle in r-ϕ between the di-muons be less than $130°$.

E. Luminosity

The CLC counters monitor the average number of inelastic $p\bar{p}$ interactions in each bunch crossing. The inelastic $p\bar{p}$ cross section has been measured to be $\sigma_{\mathrm{in}} \sim 60$ mb by several experiments at $\sqrt{s} = 1800\,\mathrm{GeV}$ [32–34]. The inelastic $p\bar{p}$ cross section at $\sqrt{s} = 1960\,\mathrm{GeV}$ is scaled from previous measurements using the calculations in [35]. The rate of inelastic $p\bar{p}$

interactions is given by

$$\mu \cdot f_{\rm BC} = \sigma_{in} \cdot \mathcal{L}, \tag{2}$$

where $\mathcal{L}$ is the instantaneous luminosity, μ is the average number of inelastic $p\bar{p}$ interactions per bunch crossing, and $f_{\rm BC}$ is the rate of bunch crossings. In this paper, we use data from the beginning of the CDF Run II operation where the average instantaneous luminosities were relatively low.

The number of $p\bar{p}$ interactions in a bunch crossing follows Poisson statistics where the probability of empty crossings is given by $\mathcal{P}_0(\mu) = e^{-\mu}$. An empty crossing is observed when there are fewer than two counters with signals above threshold in either module of the CLC. The measured fraction of empty bunch crossings is corrected for the CLC acceptance and the value of μ is calculated. The measured value of μ is combined with the inelastic $p\bar{p}$ cross section to determine the instantaneous luminosity using Equation 2. Because this method depends only weakly on the CLC thresholds, it functions particularly well at low luminosities where the probability of empty bunch crossings is large. The systematic error on the luminosity measurement is estimated to be 6%.

In CDF Run II, only runs with greater than 10 nb^{-1} integrated luminosity are considered for analysis. Runs with good operating conditions in the detector are tagged by the online shift crews. Data from those runs are examined to exclude ones with COT, muon or trigger hardware problems. For the measurement presented in this paper, the data collected from February to July 2002 was used. This sample corresponds to a total integrated luminosity of 39.7 ± 2.3 pb^{-1}.

For J/ψ candidates with transverse momenta in the range 0 to 2 GeV/c, we use 14.8 ± 0.9 pb^{-1} of our data sample, which corresponds to that fraction of the data collected when no cut on the di-muon opening angle in the Level 3 trigger was used.

III. DATA SELECTION AND RECONSTRUCTION

A. Data selection

The events selected by the J/ψ trigger are reconstructed offline, taking advantage of the most refined constants and algorithms. We reconstruct $J/\psi \to \mu^+\mu^-$ decays by selecting events with two oppositely charged muon candidates reconstructed in the COT and CMU detectors. The $J/\psi \to \mu^+\mu^-$ sample used for this analysis was collected using the CMU di-muon triggers. Events are required to have satisfied the Level 1 and Level 3 di-muon trigger criteria.

In addition to the default muon selection criteria outlined earlier, we require a p_T independent track-stub matching criterion $\chi^2(\Delta r\phi) < 9$. A track-stub matching quality criterion $\chi^2(\Delta r\phi)$ with a one degree of freedom is calculated from $\Delta r\phi$ and the expected multiple scattering for a track of given p_T obtained from a GEANT simulation [37] of the CDF Run II detector material. We require both muons to have transverse momenta $p_T > 1.5$ GeV/c as measured offline. The trigger requirements are verified for the offline-reconstructed candidates. In addition, each CMU stub matched to a triggered stub must lie within the XTRP search window set by the Level 1 triggered track. Furthermore, track momentum is corrected for energy loss due to specific ionization and multiple scattering according to our accounting of the detector materials. We calculate the J/ψ candidate invariant mass from the four-momenta of the two muons. For a portion of the data sample under consideration, a temporary hardware problem with the di-muon logic caused the trigger to exclude J/ψ events where both muon stubs fell in the ϕ range of $240 - 270°$. Therefore, we exclude J/ψ events where both muons fall in that ϕ region and account for this in the detector acceptance. We also reject J/ψ candidates if one of the tracks passes within 1.5 cm of the center of any COT wire planes, where the trigger efficiency is difficult to model because of the distortion of the electric field due to the mechanical spacers. This exclusion is accounted for in the acceptance calculation. The muon reconstruction efficiency is measured in each of the 48 CMU detector wedges. We find that the hit efficiency in the CMU wedge on the west side of the detector covering the region $240° < \phi < 255°$ is lower due to a known hardware problem and exclude J/ψ events where either muon stub is reconstructed in this wedge. As shown in Fig. 1, there are 299800 ± 800 J/ψ events that passed these selection conditions.

To determine the yield in each J/ψ p_T bin, the di-muon invariant mass distributions are fitted using invariant mass line shapes including the radiative tail from internal bremsstrahlung obtained from a tuned hit-level COT simulation. The simulated J/ψ events are decayed using the J/ψ radiative decay model in the QQ decay package [38]. The COT hit multiplicity per track is tuned to match the data as closely as possible. The COT hit resolution is then tuned to find the best χ^2 in a binned fit to the data using the Monte Carlo invariant mass line shape for the signal and a polynomial shape for the background. Finally,

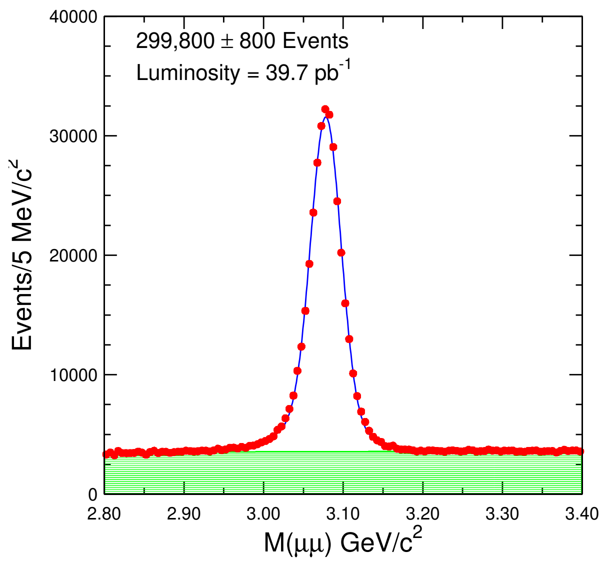

FIG. 1: Mass distribution of reconstructed di-muon J/ψ candidates. The points are data. The solid line is the fit to the signal approximated as a double Gaussian and a linear fit for the background. The hatched region is the fitted background. The fit gives a signal of 299800 ± 800 J/ψ events with an averaged mass of $3.09391 \pm 0.00008\,\mathrm{GeV}/c^2$ obtained and an average width of $0.020 \pm 0.001\,\mathrm{GeV}/c^2$ mainly due to detector resolution. The uncertainties here are statistical only.

energy loss and multiple scattering in material encountered before the COT are modeled. The energy loss in the silicon material is scaled until the peaks of the di-muon invariant mass distribution in different p_T ranges in data and from the simulation match. The order of the background polynomial used varies with the background shape in each J/ψ p_T range. A third-order polynomial is used for the momentum range 0-0.25 GeV/c, a second-order polynomial is used for the range 0.25-2.25 GeV/c, and a first-order polynomial (linear background) for transverse momenta greater than 2.25 GeV/c. The fits to the invariant mass distributions in four J/ψ p_T ranges are shown in Figs. 2. The J/ψ yields and the statistical uncertainties obtained from the fits in each p_T range are listed in the first column of Table I. The mass fitting qualities in all p_T bins are good as indicated from the fit probability shown in these Figures. We also examined the differences between counting the event numbers in the J/ψ signal region ($3.02 \to 3.15\,\mathrm{GeV}/c^2$) to that predicted from the fitting functions of signal and background. The differences ranging from +9% in the lowest p_T bin to -1.3% in the high p_T bin are used very conservatively as the systematic uncertainties from the mass fitting.

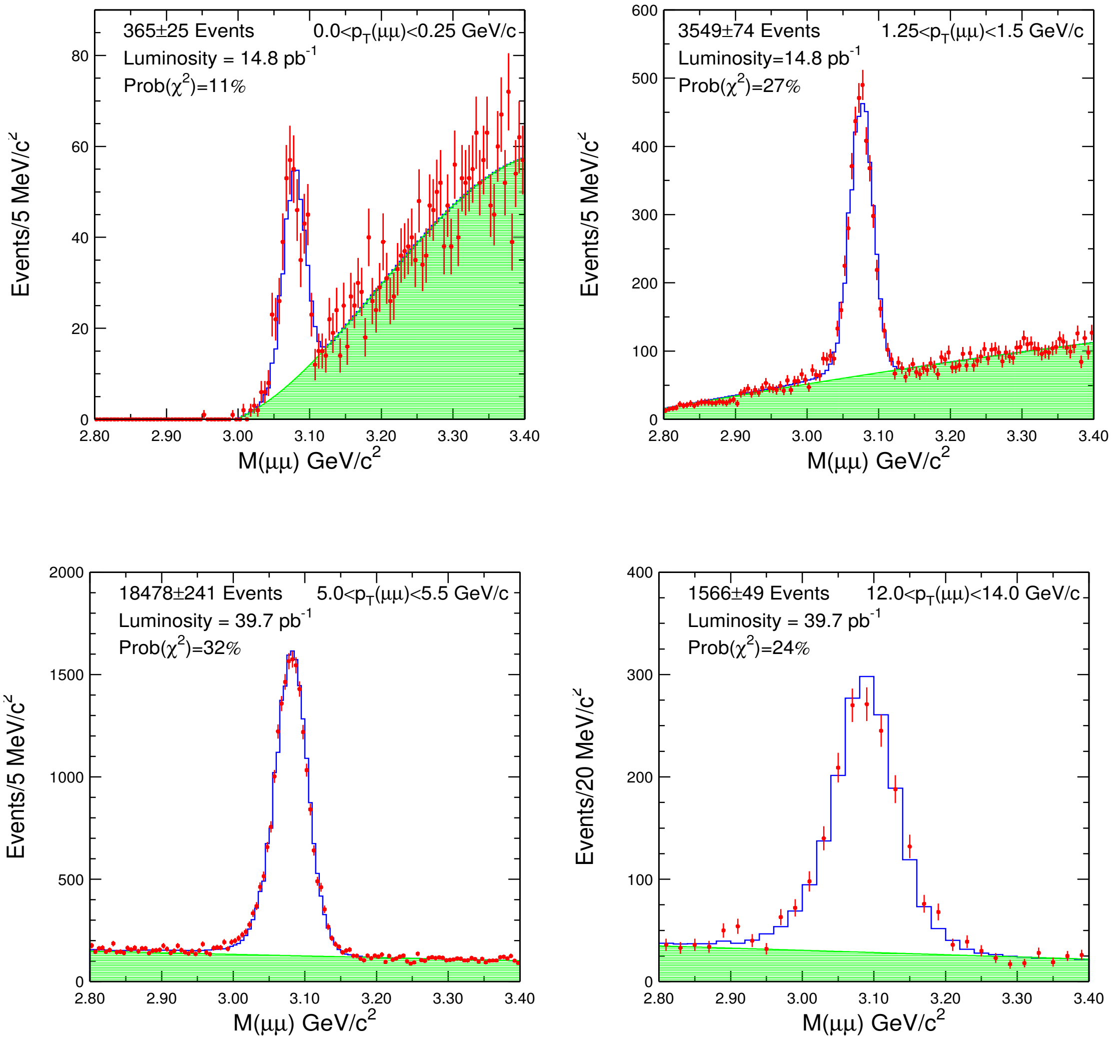

FIG. 2: Invariant mass distributions of reconstructed $J/\psi \to \mu\mu$ events in the ranges of $p_T(\mu\mu) < 0.25\,\mathrm{GeV}/c$ (top left), $1.25 < p_T(\mu\mu) < 1.5\,\mathrm{GeV}/c$ (top right), $5.0 < p_T(\mu\mu) < 5.5\,\mathrm{GeV}/c$ (bottom left) and $12.0 < p_T(\mu\mu) < 14.0\,\mathrm{GeV}/c$ (bottom right). The points with error bars are data. The solid line is the fit to the signal shape from the simulation and a polynomial shape for the background. The shaded histogram is the fitted background shape. The number of signal events and the fit probability of the binned χ^2 fitting are also provided.

TABLE I: Summary of the inclusive J/ψ cross-section analysis components. The values of the yield and statistical uncertainty from the fits are listed in the 2nd column. The acceptance values and the combined systematic and statistical uncertainties on the acceptance are listed in the 3rd column. In the 4th and 5th columns the trigger and track-stub matching efficiencies obtained from the mean of the distribution in each bin and the corresponding systematic uncertainties are listed. The sixth column lists the integrated luminosity used for each measurement.

P_t range GeV/c	Yield (N^i)	Acceptance ($\mathcal{A}^i$)	Level 1 Trigger Efficiency (ϵ^i_{L1})	Track-stub matching Efficiency($\epsilon^i_{\chi^2}$)	Luminosity ($\mathcal{L}^i$) nb^{-1}
$0.0-0.25$	365 ± 25	0.0153 ± 0.0007	0.857 ± 0.013	0.9963 ± 0.0009	14830 ± 870
$0.25-0.5$	605 ± 30	0.0069 ± 0.0004	0.860 ± 0.013	0.9963 ± 0.0009	"
$0.5-0.75$	962 ± 38	0.0070 ± 0.0004	0.865 ± 0.013	0.9962 ± 0.0009	"
$0.75-1.0$	1592 ± 49	0.0087 ± 0.0005	0.871 ± 0.014	0.9961 ± 0.0009	"
$1.0-1.25$	2500 ± 62	0.0116 ± 0.0006	0.877 ± 0.014	0.9960 ± 0.0009	"
$1.25-1.5$	3549 ± 74	0.0151 ± 0.0008	0.885 ± 0.014	0.9957 ± 0.0009	"
$1.5-1.75$	4517 ± 84	0.0190 ± 0.0009	0.892 ± 0.014	0.9955 ± 0.0009	"
$1.75-2.0$	5442 ± 93	0.0232 ± 0.0011	0.899 ± 0.015	0.9953 ± 0.0009	"
$2.0-2.25$	16059 ± 167	0.0271 ± 0.0013	0.905 ± 0.015	0.9960 ± 0.0009	39700 ± 2300
$2.25-2.5$	18534 ± 252	0.0317 ± 0.0015	0.911 ± 0.015	0.9946 ± 0.0009	"
$2.5-2.75$	18437 ± 253	0.0367 ± 0.0017	0.916 ± 0.015	0.9943 ± 0.0009	"
$2.75-3.0$	18858 ± 259	0.0415 ± 0.0019	0.920 ± 0.015	0.9939 ± 0.0009	"
$3.0-3.25$	18101 ± 253	0.0467 ± 0.0021	0.924 ± 0.015	0.9935 ± 0.0009	"
$3.25-3.5$	17597 ± 250	0.0532 ± 0.0024	0.927 ± 0.015	0.9931 ± 0.0009	"
$3.5-3.75$	16400 ± 241	0.0576 ± 0.0025	0.930 ± 0.015	0.9927 ± 0.0009	"
$3.75-4.0$	14863 ± 226	0.0628 ± 0.0029	0.932 ± 0.015	0.9923 ± 0.0009	"
$4.0-4.25$	14056 ± 218	0.0694 ± 0.0031	0.934 ± 0.015	0.9918 ± 0.0010	"
$4.25-4.5$	12719 ± 212	0.0768 ± 0.0034	0.936 ± 0.015	0.9913 ± 0.0010	"
$4.5-4.75$	12136 ± 201	0.0840 ± 0.0037	0.937 ± 0.014	0.9909 ± 0.0010	"
$4.75-5.0$	10772 ± 188	0.0904 ± 0.0039	0.939 ± 0.014	0.9904 ± 0.0010	"
$5.0-5.5$	18478 ± 241	0.1006 ± 0.0042	0.940 ± 0.014	0.9897 ± 0.0010	"
$5.5-6.0$	14616 ± 210	0.1130 ± 0.0046	0.942 ± 0.014	0.9887 ± 0.0011	"
$6.0-6.5$	11388 ± 180	0.1257 ± 0.0051	0.946 ± 0.014	0.9876 ± 0.0011	"
$6.5-7.0$	8687 ± 154	0.1397 ± 0.0055	0.945 ± 0.014	0.9865 ± 0.0012	"
$7.0-8.0$	12409 ± 139	0.1561 ± 0.0068	0.946 ± 0.014	0.9850 ± 0.0012	"
$8.0-9.0$	6939 ± 107	0.1723 ± 0.0075	0.947 ± 0.014	0.9827 ± 0.0013	"
$9.0-10.0$	3973 ± 78	0.1807 ± 0.0079	0.948 ± 0.014	0.9804 ± 0.0014	"
$10.0-12.0$	3806 ± 74	0.1938 ± 0.0074	0.949 ± 0.014	0.9772 ± 0.0016	"
$12.0-14.0$	1566 ± 49	0.2163 ± 0.0081	0.960 ± 0.014	0.9726 ± 0.0017	"
$14.0-17.0$	935 ± 40	0.238 ± 0.011	0.951 ± 0.014	0.9671 ± 0.0018	"
$17.0-20.0$	350 ± 25	0.247 ± 0.012	0.951 ± 0.014	0.9600 ± 0.0020	"

IV. ACCEPTANCE AND EFFICIENCY

A. Monte Carlo Description

We use the GEANT [37] Monte Carlo simulation software to estimate the geometric and kinematic acceptances. The variation of detector conditions in the simulation is set to match the data. J/ψ events are generated starting with a kinematic distribution that is flat in rapidity and with a p_T distribution selected to best match the reconstructed data. The events are fully simulated. After the differential cross section is measured, we iterate and recalculate the acceptance and the central value of the cross section using the measured p_T distribution. The GEANT simulation is validated by comparing the resulting distributions of various kinematic quantities such as η, p_T, the track-stub matching distance, and the z vertex distribution in reconstructed data and reconstructed Monte Carlo events. Differences in the data and Monte Carlo distributions are used to estimate the systematic uncertainties on the modeling of the CDF detector geometry in the simulation.

B. Acceptance

We correct the observed number of J/ψ events for the detector acceptance and efficiency. The CMU muon detector covers the pseudo-rapidity range of $\mid \eta \mid < 0.6$. In this region the coverage of the COT is complete and the CDF detector acceptance is driven by the muon detector geometry and kinematic reach. The calorimeter acts as an absorber for the CMU detector which is therefore sensitive only to muons with $p_T > 1.35$ GeV/c. The arrangement of the four sense wires within the CMU chambers allows a lower bound on the transverse momentum of the muon to be calculated from the difference in drift times in sense wires on alternating layers. The $\Delta t \leq 396$ ns timing window is selected to be fully efficient for muons with $p_T > 1.5\,\mathrm{GeV}/c$.

The acceptance is modeled as a function of both the reconstructed $p_T(J/\psi)$ and rapidity $y(J/\psi)$ and is defined as the ratio between the number of generated events N^{gen} and recontructed events N^{rec},

$$\mathcal{A}(p_T, y) = \frac{N^{rec}(p_T(J/\psi), |y(J/\psi)| < 0.6)}{N^{gen}(p'_T(J/\psi), |y'(J/\psi)| < 0.6)}, \tag{3}$$

where $p'_T(J/\psi)$ and y' are the generated true values of the J/ψ momentum and rapidity.

The acceptance as a function of p_T and y is shown in Fig. 3.

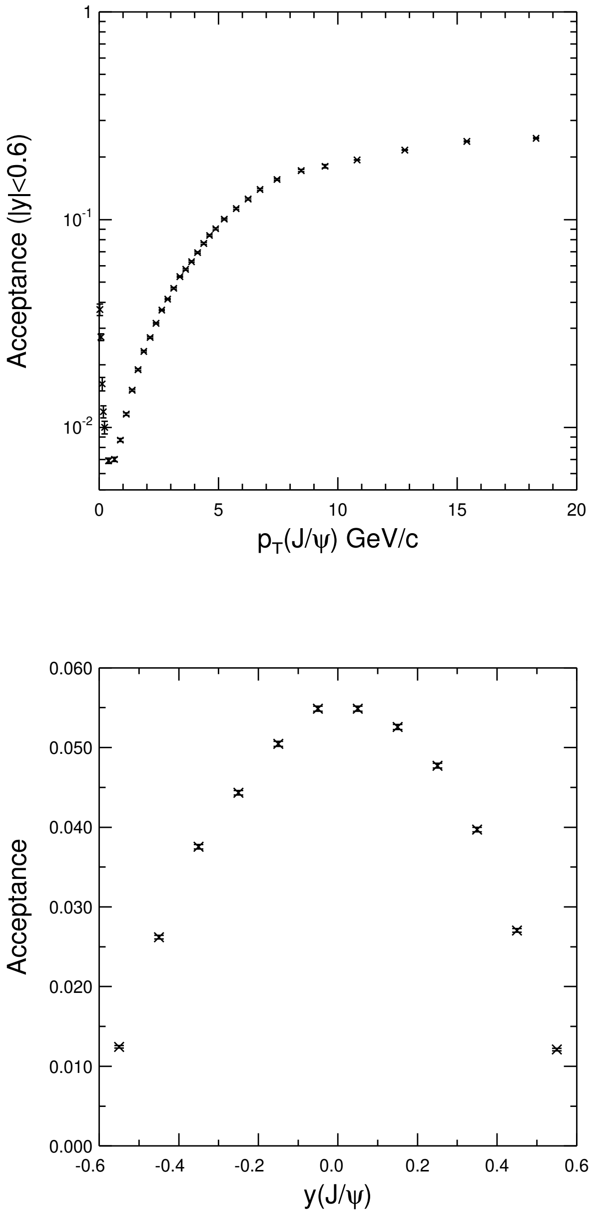

FIG. 3: Acceptance of $J/\psi \to \mu\mu$ events determined from a GEANT simulation of the CDF detector. The acceptance is shown as a function of $p_T(J/\psi)$ and $y(J/\psi)$. The acceptance as a function of $p_T(J/\psi)$ is measured integrated over $|y| < 0.6$ and the acceptance as a function of y is shown integrated over all p_T.

The acceptance increases rapidly from 0.7% at $p_T = 0.25\,\mathrm{GeV}/c$ to 10% at $5\,\mathrm{GeV}/c$

and 25% at 20 GeV/c. The acceptance in the range 0.0-0.25 GeV/c is rapidly varying as a function of $p_T(J/\psi)$ and increases with decreasing momenta from 0.7% at $p_T(J/\psi) = 0.25$ GeV/c to 4% for J/ψ mesons almost at rest ($p_T < 50$ MeV/c). The muon transverse momentum is required to be greater than or equal to 1.5 GeV/c, which is close to one-half of the J/ψ mass, therefore when the J/ψ is at rest both muons are likely to be above the p_T threshold. As soon as the J/ψ receives a small boost, the probability is greater that at least one muon will be below the p_T acceptance threshold and the acceptance starts to decrease until the J/ψ transverse momentum exceeds 0.25 GeV/c.

There is a small but non-zero acceptance at $|y| = 0.6$ due to detector resolution and the size of the interaction region. J/ψ Monte Carlo events generated with a flat rapidity distribution in the range $|y|_{\rm gen} < 1.0$ and a p_T distribution as described in Section IV A are simulated. The relative acceptance of events generated with $|y|_{\rm gen} > 0.6$ and reconstructed with $|y|_{\rm reco} < 0.6$, $\mathcal{A}'$, is calculated thus:

$$\mathcal{A}' = \frac{N^{\rm rec}(|y|_{\rm gen} > 0.6, |y|_{\rm rec} < 0.6)}{N^{gen}(|y|_{\rm gen} < 0.6)}, \tag{4}$$

where $N^{\rm rec}(|y|_{\rm gen} > 0.6, |y|_{\rm rec} < 0.6)$ is the number of J/ψ events in the Monte Carlo sample with reconstructed $|y|_{\rm reco} < 0.6$ and generated $|y|_{\rm gen} > 0.6$ and $N^{gen}(|y|_{\rm gen} < 0.6)$ is the total number of events generated with $|y| < 0.6$. The value of $\mathcal{A}'$ is found to be very small: $\mathcal{A}' = 0.00071 \pm 0.00006(stat)$. A correction factor of $(1 - \mathcal{A}') = 99.93\%$ is applied to the J/ψ yield calculated in each $p_T(J/\psi)$ bin.

A 2-dimensional acceptance function was used for an event-by-event correction during the cross section calculation process. In Table I, the averaged acceptance values and the combined statistical and systematic uncertainties for each p_T bin are given. Sources of systematic uncertainties studied are J/ψ spin alignment, p_T spectrum, CMU simulation and detector material description in GEANT simulation.

Kinematic acceptance as a function of p_T depends on the J/ψ spin alignment. The normalized alignment distribution is given by

$$I(\theta) = \frac{3}{2(\alpha + 3)}(1 + \alpha \cos^2 \theta), \tag{5}$$

where θ is the angle between the muon in the J/ψ rest frame and the direction of the J/ψ in the lab frame [5] and α quantifies the spin alignment. The parameter α must lie in the range -1 to 1 and $\alpha = 0$ indicates no preferred spin alignment. The previous CDF measurements of the J/ψ spin alignment parameter [5] are consistent with zero but could also be as large as 50% in some p_T regions. The weighted mean of α measured in different p_T ranges in [5] is used to determine the central value of the parameter α to be used for the acceptance. The value of $\alpha = 0.13 \pm 0.15$ is used for the final acceptance values where the uncertainty is chosen to accommodate the variation in the previous CDF measurements and the extrapolation to $p_T = 0$ where α is expected to be zero. The uncertainty on acceptance due to spin alignment is largest in the lower momentum bins and decreases with increasing transverse momentum. We find the uncertainty is $\sim 5\%$ near $p_T = 0$ and 2% in the region $17 < p_T < 20\,\mathrm{GeV}/c$.

To estimate the uncertainty from variations of the input transverse momentum spectrum, the acceptance is recalculated using a Monte Carlo sample generated using a flat distribution. The flat distribution is an extreme alternative from the nominal spectrum which is a fast falling function of p_T. The fractional change in acceptance is taken as the uncertainty on the input transverse momentum distribution. The uncertainty is about 3% in the lowest momentum bin, less than 1% in the 0.25 to $3\,\mathrm{GeV}/c$ bins, 1-2% in the 3 to $4\,\mathrm{GeV}/c$ bins, and 2-4% in the 4 to 20 GeV/c bins.

A systematic error of 1.0% from uncertainties related to the CMU chamber simulation is estimated by comparing event distributions in data and in Monte Carlo. The modeling of the CMU coverage in the r-z plane, the wire efficiency differences between wedges in east and west and in different ϕ sections, and beam position in z are found to be the major sources of the simulation uncertainties.

There is a gap in CMU coverage in the central region of the detector in the r-z plane. The gap in coverage is approximately ± 11 cm, measured at a radius of 347 cm. The fraction of muons falling in the gap region but still accepted by the CMU due to multiple scattering is compared between data and Monte Carlo. The deviation between the ratios in data and Monte Carlo is taken as the uncertainty in the modeling of the CMU fiducial volume in the center of the CDF detector. The uncertainty is found to be 0.20%.

Several factors contribute to the difference in the numbers of J/ψ mesons with decay vertex in the opposite halves of the detector along z. These include the shift in the average primary vertex location towards positive z (east), the exclusion of the low efficiency wedge on the west side of the detector, and the uncertainty in the modeling of the z extent of the CMU detector, as well as the differences in the east and west chambers. We found a difference of 0.80% between data and Monte Carlo on the east-west asymmetry in the number of reconstructed J/ψ events.

The ϕ acceptance of the CMU detector obtained from the GEANT simulation does not include the differences in gain and efficiencies between wedges. The number of events reconstructed in each wedge in data and Monte Carlo is examined and the total number of events in Monte Carlo is normalized to match the data. The standard deviation of the difference between the number of events reconstructed in each wedge between data and Monte Carlo is taken as the uncertainty on the CMU ϕ acceptance. We find an uncertainty of 0.55% due to this source.

Muons from J/ψ are required to have the z_0 position to be within 90 cm of the center of the detector, $|z_0| < 90$ cm. There is a small disagreement between the data and the Monte Carlo in the $z_0(\mu)$ distributions due to inadequate modeling of the interaction region. This contribution to the systematic error is estimated from the difference between the ratios of data and Monte Carlo tracks with $|z_0| < 90\,\mathrm{cm}$ compared to all muons. We find an uncertainty of 0.28%.

The material description of the CDF detector in GEANT determines the amount of energy loss from a muon track when it travels through the detector. Inside the tracking volume, the material description of the new silicon detector has the biggest impact on muon tracks in the low momentum range which is of special interest to this analysis. To estimate the systematic error on the acceptance from uncertainty of the detector material description, the SVX II material used in the simulation was varied by 10 % to 20%. The systematic uncertainty is taken as the difference between the acceptance values measured with different material scale factors and the nominal. The uncertainty is largest in the low momentum bins where it is around 5%.

The systematic uncertainties on acceptance are summarized in Table IV. The size of the uncertainties from J/ψ spin alignment, J/ψ p_T spectrum and detector material description depends on the muon p_T range as expected while the uncertainty from muon detector simulation is the same for all p_T ranges of interests in the analysis.

C. Data Quality

The yield, mean, and resolution of the J/ψ invariant mass peak were monitored over the period of the data taking to evaluate the detector performance. The number of J/ψ mesons reconstructed is normalized by the integrated luminosity of each run. We identify outlying runs which may have additional hardware or trigger problems that have been undetected by the standard offline validation procedures. Runs with J/ψ yields different by 4σ from the average, where σ is the standard deviation of the yields in a given run range, are considered outliers. Two such runs were found out of 457 considered. The integrated luminosities of these two runs are 14.3 nb^{-1} and 258.3 nb^{-1}. Further investigations of online operational conditions during these runs revealed no obvious hardware or trigger malfunctions. Since the probability is 1% that a data subsample of 258.3 nb^{-1} out of a total sample of 39.7 pb^{-1} would have a yield different by $> 4\sigma$, both runs are included in the baseline cross-section measurement. The measurement is repeated without the outlier runs included and a systematic uncertainty assigned from the difference in the measurements. We find the uncertainty on the total cross section to be less than 1%.

D. Trigger Efficiency

For our measurement of the Level 1 di-muon trigger efficiency, we used J/ψ events that were taken with a high-p_T single-muon trigger. At Level 1, this trigger requires a muon with p_T greater than $4.0\,\mathrm{GeV}/c$. In Level 3, a J/ψ is reconstructed using the triggered high-p_T muon and a second muon which is not required to pass the Level 1 requirements. This second muon is then used to measure the Level 1 single-muon efficiency. The denominator of the efficiency measurement is the number of J/ψ reconstructed using the Level 3 track and muon information. These J/ψ candidates must have a mass between 2.7 and 3.6 GeV/c^2, a di-muon opening angle of $\Delta\phi_0 < 130°$, and a separation in z_0 of less than 5 cm between the candidate's tracks. The probe-muon track must have at least 20 COT axial-layer hits and 16 COT stereo-layer hits, a CMU r-ϕ match of $\chi^2(\Delta r\phi) < 9$, and a track $|z_0| < 90\,\mathrm{cm}$. Tracks are excluded if they pass within 1.5 cm of the center of any of the COT wire planes in any of the axial layers in order to avoid the inefficient region caused by wire supports. For the probe muon to pass the Level 1 trigger, the associated Level 3 track must be matched to an XFT track and the Level 3 CMU stub must be matched to a Level 1 CMU stub that lies within XTRP window. The resulting Level 1 muon-finding efficiency is shown in Fig. 4. The distribution is fit to the following function:

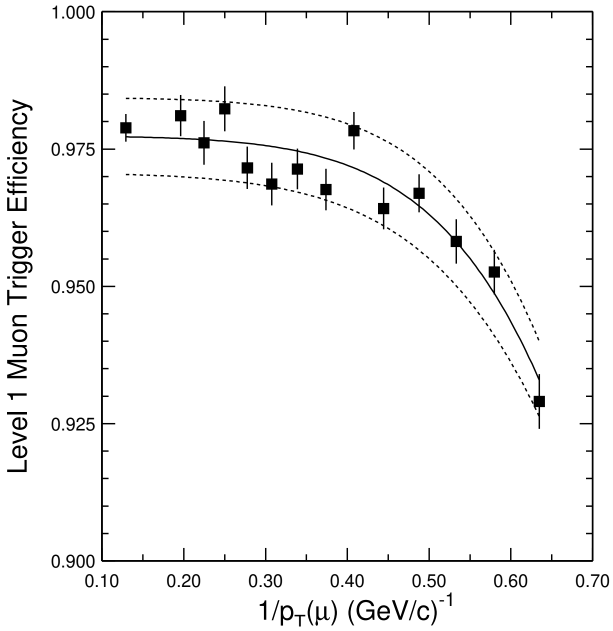

FIG. 4: The Level 1 CMU trigger efficiency as a function of muon p_T. Points with error bars are measurement points. The solid line is the fitting result using the function described in the text. The dashed lines indicate the range used to determine the uncertainty.

$$\epsilon^{\mu}_{\mathrm{L1}}(p^{\mu}_{T}) = E \cdot \mathrm{freq}\left(\frac{A - 1/p_T}{R}\right), \tag{6}$$

where freq is the normal frequency function:

$$\mathrm{freq}(x) = \frac{1}{\sqrt{2\pi}} \int_{-\infty}^{x} e^{-\frac{1}{2}t^2} dt, \tag{7}$$

E is the plateau efficiency, A is associated with the p_T at which the efficiency is half the peak value, and R is the effective Gaussian resolution. We find $E = 0.977 \pm 0.002$, $A = 1.1 \pm 0.1$ $(\mathrm{GeV/c})^{-1}$, and $R = 0.28 \pm 0.06$ $(\mathrm{GeV/c})^{-1}$.

To determine the uncertainty in the Level 1 trigger efficiency, while also taking into account the data fluctuations around the central fit as shown in Fig. 4, the range of the uppermost and lowermost fluctuations supported by the data are computed as follows: $x'(p_T) = \bar{x} \pm (|x - \bar{x}| + 1\sigma)$ where x is the data value, $\bar{x}$ is the value returned by the fit and σ is the uncertainty on the data. The $x'(p_T)$ distribution is refit using the function in Equation 6. The results are shown as dashed lines in Fig. 4. The di-muon Level 1 trigger efficiency is calculated on an event-by-event basis to take into account μ-μ correlations. For each J/ψ candidate, the Level 1 J/ψ reconstruction efficiency is given by:

$$\epsilon_{\rm L1}^{J/\psi}(p_T^{J/\psi}) = \epsilon_{\rm L1}^{\mu}(p_T^{\mu_1}) \cdot \epsilon_{L1}^{\mu}(p_T^{\mu_2}), \tag{8}$$

where $\epsilon_{\rm L1}^{\mu}(p_T^{\mu})$ is the single muon Level 1 trigger efficiency given by Equation 6, and $p_T^{\mu_{1,2}}$ are the transverse momenta of the two muon candidates. The trigger's exclusion of pairs with nearby stubs is included as part of the geometric acceptance. The mean of the Level 1 di-muon trigger efficiency distribution in each J/ψ transverse momentum bin is listed in Table I. The maximum difference from varying the trigger efficiencies by one standard deviation independently for the two muons is listed as the uncertainty on the di-muon trigger in Table I. We find that the variation is within $\pm 1.5\%$ in all bins.

The Level 3 reconstruction efficiency is dominated by the difference between the online and offline tracking efficiency. A fast tracking algorithm is used for pattern recognition in the COT in Level 3. In the offline reconstruction a more accurate tracking algorithm is combined with the result of the Level 3 algorithm to give a higher overall COT tracking efficiency. The Level 3 single-muon reconstruction efficiency as measured versus the offline reconstruction algorithm is found to be constant for $p_T(\mu) > 1.5\,{\rm GeV}/c$ and is

$$\epsilon_{\rm L3/Offline}^{\mu} = 0.997 \pm 0.001(stat) \pm 0.002(syst). \tag{9}$$

In the Level 3 trigger, the muons are required to be separated in z_0 by less than 5 cm. The efficiency $\epsilon_{\Delta z_0}$ of this cut is measured using J/ψ candidates reconstructed in single-muon-trigger data samples where a Level 3 di-muon trigger was not required to acquire the data. The numbers of events that passed the z_0-separation criterion in the mass signal and sideband regions are examined. The cut is found to be 100% efficient with an uncertainty of 0.1%. The uncertainty is driven by the statistical limitations of the small data samples obtained from the single-muon triggers.

E. Reconstruction Efficiencies

The COT tracking efficiency was measured using a Monte Carlo track embedding technique. Hits from simulated muon tracks are embedded into CDF Run II di-muon events.

The distance resolution and hit-merging distance are adjusted so the embedded track has residuals and hit distributions matched to muon tracks in J/ψ data events. The efficiency of COT track reconstruction in di-muon events is found to be

$$\epsilon_{\mathrm{COT}}(p_T^\mu > 1.5\,\mathrm{GeV}/c) = 0.9961 \pm 0.0002(stat)^{+0.0034}_{-0.0091}(syst). \quad (10)$$

The absolute offline reconstruction efficiency of muons including stub reconstruction and matching stubs to tracks is measured using J/ψ events from single-muon trigger samples where the J/ψ invariant mass is reconstructed from a triggered, fully-reconstructed muon and a second track. Tracks from the di-muon-mass signal region are projected to the muon chambers, and the efficiency of finding a matched stub is measured. For muons in the CMU fiducial region with $p_T(\mu) > 1.5\,\mathrm{GeV}/c$, the offline reconstruction efficiency is found to be independent of p_T and is measured to be:

$$\epsilon^\mu_{\mathrm{CMU}} = 0.986 \pm 0.003 \pm 0.010. \quad (11)$$

To select clean CMU muons, the track-stub matching in the r-ϕ plane is required to have $\chi^2(\Delta r\phi) < 9$. The efficiency of this cut is found to have a weak dependence on p_T^μ:

$$\epsilon_{\chi^2} = (1.0018 \pm 0.0003) - (0.0024 \pm 0.0001)p_T^\mu. \quad (12)$$

The efficiency of the track-stub matching criterion ($\chi^2(\Delta r\phi) < 9$) as a function of J/ψ transverse momentum, obtained using an event-by-event weighting is listed in Table I. The systematic uncertainty on the weighted-average matching-cut efficiency is obtained by varying the normalization and slope in Equation 12 by one standard deviation. The change in the weighted average efficiency in each J/ψ transverse momentum bin is found to be $\leq 0.2\%$.

Since the two muons originate from a common decay point, the efficiency of the track z_0 cut is fully correlated for the two muons and is counted only once. The combined p_T independent COT-tracking, muon and Level 3 reconstruction efficiencies for J/ψ mesons is calculated to be

$$\epsilon_{\mathrm{rec}} = \epsilon^2_{L3} \cdot \epsilon^2_{COT} \cdot \epsilon^2_{\mathrm{CMU}} \cdot \epsilon_{z_0} \cdot \epsilon_{\Delta_{z_0}} = 95.5 \pm 2.7\%. \quad (13)$$

Table II summarizes the p_T-independent reconstruction efficiencies and those of the various muon selection cuts.

TABLE II: Summary of J/ψ reconstruction efficiencies.

J/ψ Selection	Efficiency
Level 3 muon reconstruction	$\epsilon_{L3} = 0.997 \pm 0.001 \pm 0.002$
COT offline tracking	$\epsilon_{COT} = 0.9961 \pm 0.0002^{+0.0034}_{-0.0091}$
Muon offline reconstruction	$\epsilon_{CMU} = 0.986 \pm 0.003 \pm 0.010$
Muon z_0 position less than ± 90 cm	$\epsilon_{z_0} = 0.9943 \pm 0.0016$
Di-muon z_0 separation less than 5 cm	$\epsilon_{\Delta z_0} = 1.0 \pm 0.001$
Total reconstruction	$\epsilon_{rec} = \epsilon^2_{L3} \cdot \epsilon^2_{COT} \cdot \epsilon^2_{CMU} \cdot \epsilon_{z_0} \cdot \epsilon_{\Delta z_0} = 95.5 \pm 2.7\%$

V. J/ψ CROSS SECTION

An event-by-event weighting is used to determine the J/ψ yield in each p_T bin. Each event is weighted using the Level 1 single muon efficiency $\epsilon_{\rm L1}(p_T^\mu)$ and the efficiency of the track-stub matching criterion $\epsilon_{\chi^2}(p_T^\mu)$ applied to each of the two muons. The event is then corrected for the acceptance $\mathcal{A}(p_T^{J/\psi}, y^{J/\psi})$. The weight of each candidate event is given by:

$$\begin{aligned} 1/w_i = \quad & \epsilon_{\rm L1}(p_T^{\mu 1}) \cdot \epsilon_{L1}(p_T^{\mu 2}) \cdot \\ & \epsilon_{\chi^2}(p_T^{\mu 1}) \cdot \epsilon_{\chi^2}(p_T^{\mu 2}) \cdot \mathcal{A}(p_T^{J/\psi}, y^{J/\psi}). \end{aligned} \tag{14}$$

We fit the invariant mass distributions of the weighted events, using the same shapes for signal and background as shown in Fig. 2. The number of signal events in each transverse momentum bin is determined from the area under the signal mass peak. The error on the corrected yield from the mass template fit, $N(p_T)_{\rm corrected}$ is given by:

$$\delta(N(p_T)_{\rm corrected}) = \sqrt{\sum_{i=0}^{i=N_s} (w_i)^2}, \tag{15}$$

where N_s is the raw number of signal events in each momentum bin before weighting. In a similar fashion, the di-muon p_T distribution in each bin is weighted. The weighed p_T distribution of the mass sideband subtracted events in the J/ψ mass signal region is used to determine the mean p_T value for each transverse momentum bin.

The J/ψ differential cross section is then calculated as follows:

$$\frac{d\sigma}{dp_T} \cdot Br(J/\psi \to \mu\mu) = \frac{N(p_T)_{\rm corrected} \cdot (1 - \mathcal{A}')}{\epsilon_{\rm rec} \cdot \int \mathcal{L}dt \cdot \Delta p_T}, \tag{16}$$

where $d\sigma/dp_T$ is the average cross section of inclusive J/ψ in that p_T bin integrated over $\mid y(J/\psi) \mid < 0.6$, $\mathcal{A}'$ is the correction factor for y smearing defined by Equation 4, $\epsilon_{\rm rec}$ is the combined Level 3 and offline tracking and muon reconstruction efficiency, $\int \mathcal{L}dt$ is the integrated luminosity, and Δp_T is the size of the p_T bin.

The cross-section values obtained with statistical and p_T-dependent uncertainties are listed in Table III.

An uncertainty of $+0.1\%$ on the momentum scale is extracted by comparing the reconstructed J/ψ mass as shown in Fig. 1 to the world averaged value of $3.09688 \pm 0.00004\,\mathrm{GeV}/c^2$ [22]. The 3 MeV/c^2 difference is attributed to an underestimation of the energy loss in the silicon detector due to an incomplete accounting of the material at the time the data sample used in this analysis was processed. The $+0.1\%$ uncertainty from the momentum scale corresponds to an uncertainty on the differential cross section as $d(d\sigma/dp_T)/dp_T \times 0.1\%$. Using the values in Table III, the first derivative of the differential cross section is calculated and the momentum scale uncertainty on the cross section in each bin estimated. The effect was found to be small, the largest negative deviation being -0.08% and the largest positive deviation being $+0.7\%$.

Table IV summarizes the different contributions to the systematic errors applied to the cross-section measurement from acceptance calculations using a Monte Carlo simulation, the mass line shapes used to determine the yield, the trigger and reconstruction efficiencies, and the luminosity measurement.

The differential cross-section results with systematic and statistical uncertainties are displayed in Fig. 5. The invariant cross section, $d\sigma/dp_T^2 \cdot Br(J/\psi \to \mu\mu)$, with systematic errors is shown in Fig. 6. The results are also listed in Table III.

We integrate the differential cross section to find the total J/ψ production cross section:

$$\begin{aligned} &\sigma(p\overline{p} \to J/\psi X, \mid y(J/\psi) \mid < 0.6) \cdot Br(J/\psi \to \mu\mu) \\ &= 240 \pm 1(stat)^{+21}_{-19}(syst) \text{ nb.} \end{aligned} \tag{17}$$

The p_T-dependent systematic uncertainties are summed and then added in quadrature with

TABLE III: The differential J/ψ cross section times the branching fraction $Br \equiv Br(J/\psi \to \mu\mu)$ as a function of p_T for $|y(J/\psi)| < 0.6$. For each measurement, the first uncertainty is statistical and the second uncertainty is systematic. The systematic uncertainties shown are the p_T dependent uncertainties only. The fully correlated p_T independent systematic uncertainty in each bin is 6.9%.

$p_T(J/\psi)$ (GeV/c)	Mean p_T	Mean p_T^2	$\frac{d\sigma}{dp_T} \cdot Br$ (nb/(GeV/c))	$\frac{d\sigma}{dp_T^2} \cdot Br$ (nb/(GeV/c^2))
$0.0 - 0.25$	0.15	0.027	$9.13 \pm 0.6(stat)^{+1.1}_{-0.7}(syst)$	$36.5 \pm 2.4(stat)^{+4.2}_{-2.6}(syst)$
$0.25 - 0.5$	0.39	0.16	$28.1 \pm 1.5^{+2.4}_{-1.6}$	$37.4 \pm 2.0^{+3.1}_{-2.0}$
$0.5 - 0.75$	0.64	0.42	$45.3 \pm 1.9^{+3.0}_{-2.1}$	$36.2 \pm 1.5^{+2.5}_{-1.8}$
$0.75 - 1.0$	0.89	0.79	$59.3 \pm 2.0^{+4.0}_{-2.9}$	$33.9 \pm 1.1^{+2.3}_{-1.6}$
$1.0 - 1.25$	1.13	1.29	$69.6 \pm 1.9^{+3.6}_{-3.2}$	$31.0 \pm 0.8^{+1.7}_{-1.5}$
$1.25 - 1.5$	1.38	1.91	$73.4 \pm 1.7^{+3.9}_{-3.5}$	$26.7 \pm 0.6^{+1.4}_{-1.3}$
$1.5 - 1.75$	1.63	2.66	$75.2 \pm 1.6^{+3.8}_{-3.3}$	$23.2 \pm 0.5^{+1.2}_{-1.0}$
$1.75 - 2.0$	1.87	3.52	$72.9 \pm 1.4^{+3.7}_{-3.3}$	$19.4 \pm 0.4^{+0.9}_{-0.8}$
$2.0 - 2.25$	2.13	4.53	$69.1 \pm 0.8^{+3.3}_{-2.9}$	$16.3 \pm 0.2^{+0.8}_{-0.7}$
$2.25 - 2.5$	2.38	5.65	$67.3 \pm 1.0^{+3.1}_{-2.8}$	$14.2 \pm 0.2^{+0.7}_{-0.6}$
$2.5 - 2.75$	2.62	6.89	$57.6 \pm 0.9 \pm 2.6$	$11.0 \pm 0.2 \pm 0.5$
$2.75 - 3.0$	2.87	8.26	$52.0 \pm 0.8 \pm 2.4$	$9.04 \pm 0.13 \pm 0.41$
$3.0 - 3.25$	3.12	9.76	$43.6 \pm 0.7 \pm 1.9$	$6.97 \pm 0.10 \pm 0.31$
$3.25 - 3.5$	3.38	11.4	$37.3 \pm 0.6 \pm 1.6$	$5.53 \pm 0.08 \pm 0.24$
$3.5 - 3.75$	3.62	13.1	$31.5 \pm 0.5 \pm 1.3$	$4.34 \pm 0.07 \pm 0.18$
$3.75 - 4.0$	3.87	15.0	$26.2 \pm 0.4 \pm 1.2$	$3.38 \pm 0.05 \pm 0.15$
$4.0 - 4.25$	4.12	17.0	$22.5 \pm 0.4 \pm 1.0$	$2.72 \pm 0.05 \pm 0.12$
$4.25 - 4.5$	4.38	19.2	$18.7 \pm 0.3 \pm 0.8$	$2.13 \pm 0.04 \pm 0.09$
$4.5 - 4.75$	4.62	21.4	$16.1 \pm 0.3 \pm 0.7$	$1.74 \pm 0.03 \pm 0.08$
$4.75 - 5.0$	4.88	23.8	$13.3 \pm 0.3 \pm 0.6$	$1.37 \pm 0.03 \pm 0.06$
$5.0 - 5.5$	5.24	27.5	$10.3 \pm 0.15 \pm 0.42$	$0.984 \pm 0.014 \pm 0.040$
$5.5 - 6.0$	5.74	33.0	$7.28 \pm 0.12 \pm 0.29$	$0.633 \pm 0.010 \pm 0.025$
$6.0 - 6.5$	6.24	38.9	$5.11 \pm 0.09 \pm 0.20$	$0.408 \pm 0.0069 \pm 0.016$
$6.5 - 7.0$	6.74	45.5	$3.54 \pm 0.07 \pm 0.14$	$0.262 \pm 0.0052 \pm 0.010$
$7.0 - 8.0$	7.45	55.7	$2.27 \pm 0.03 \pm 0.10$	$0.151 \pm 0.0019 \pm 0.006$
$8.0 - 9.0$	8.46	71.6	$1.14 \pm 0.02 \pm 0.05$	$0.0668 \pm 0.0011 \pm 0.0028$
$9.0 - 10.0$	9.46	89.5	$0.622 \pm 0.013 \pm 0.025$	$0.0327 \pm 0.0007 \pm 0.0013$
$10.0 - 12.0$	10.8	118	$0.278 \pm 0.006 \pm 0.011$	$0.0126 \pm 0.0003 \pm 0.0005$
$12.0 - 14.0$	12.8	165	$0.103 \pm 0.003 \pm 0.004$	$0.00398 \pm 0.00013 \pm 0.00015$
$14.0 - 17.0$	15.2	233	$0.037 \pm 0.002 \pm 0.002$	$0.00120 \pm 0.00005 \pm 0.00006$
$17.0 - 20.0$	18.3	336	$0.014 \pm 0.001 \pm 0.001$	$0.00037 \pm 0.00004 \pm 0.00002$

TABLE IV: Summary of systematic uncertainties in the inclusive J/ψ cross-section measurement. The p_T dependent uncertainties are listed in the top section of the table. In general, the p_T dependent uncertainties increase with decreasing p_T. The total is calculated from the p_T independent sources only.

	Source	Size
Acceptance	J/ψ spin alignment	$\pm(2 \to 5)\%$ (p_T)
Acceptance	p_T spectrum	$\pm(0 \to 5)\%$ (p_T)
Acceptance	Detector material	$\pm(0.4 \to 5)\%$ (p_T)
Yield	Mass fits	$(-1.3 \to +9)\%$ (p_T)
Yield	Momentum scale	$(-0.1 \to +0.7)\%$ (p_T)
Luminosity	CLC	$\pm 6.0\%$
Reconstruction	Table II	$\pm 2.8\%$
Acceptance	CMU simulation	$\pm 1.0\%$
Yield	Data quality	$\pm 1.0\%$
L1 trigger efficiency	Table I	$\pm 1.5\%$
Total	$\pm 6.9\% \oplus \delta(p_T)$	

the fully-correlated uncertainty of 6.9%:

$$\delta^{stat}_{\text{tot}\ \sigma\cdot\text{rmBr}} = \sqrt{\sum_{i=1}^{N_{\text{bins}}} (\delta_i^{stat})^2} = 1 \text{ nb} \tag{18}$$

$$\begin{aligned} \delta^{syst}_{\text{tot}\ \sigma\cdot\text{rmBr}} &= \left\{ \sum_{i=1}^{N_{\text{bins}}} \delta_i^{syst}(p_T) \right\} \oplus \pm 16 \text{ nb} \\ &= {}^{+21}_{-19} \text{ nb}, \end{aligned} \tag{19}$$

where N_{bins} is the total number of p_T bins, δ_i^{stat} is the statistical uncertainty in the cross-section measurement in the i^{th} bin, $\delta_i^{syst}(p_T)$ is the systematic uncertainty on the measurement in each p_T bin independent of the correlated systematic uncertainty of 6.9%, and $\oplus$ denotes addition in quadrature. After correcting for the $Br(J/\psi \to \mu\mu) = 5.88 \pm 0.10\%$ [22],

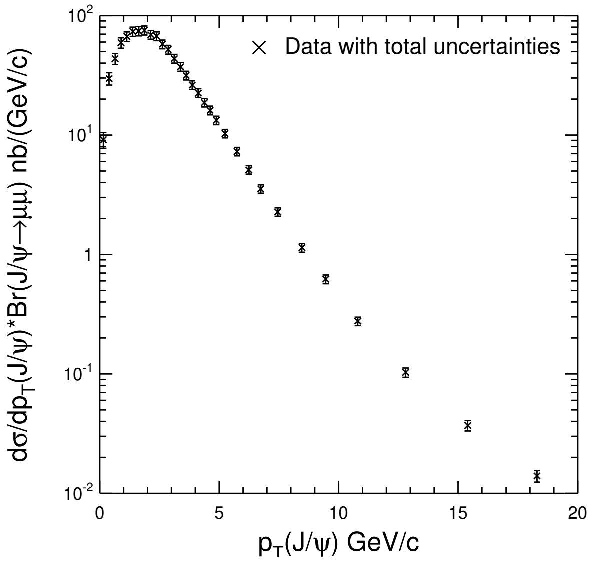

FIG. 5: Inclusive J/ψ cross section, $d\sigma/dp_T \cdot Br(J/\psi \to \mu\mu)$, as a function of J/ψ p_T integrated over the rapidity range $|y| < 0.6$. The differential cross section with systematic and statistical uncertainties added is plotted. This includes correlated uncertainties.

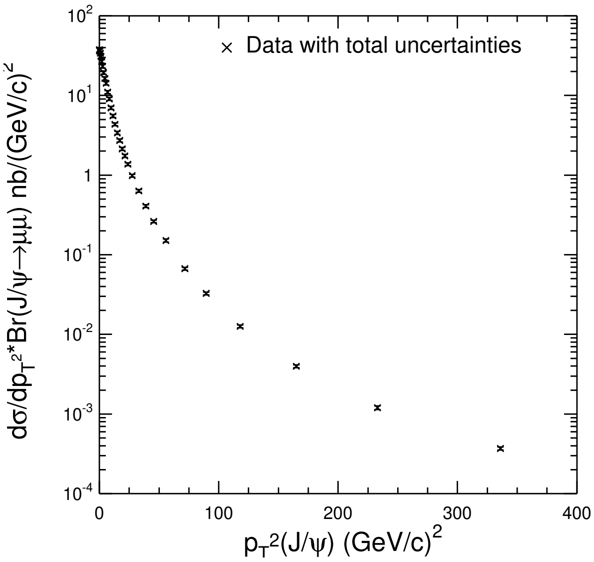

FIG. 6: The invariant J/ψ cross section, $d\sigma/dp_T^2 \cdot Br(J/\psi \to \mu\mu)$, as a function of $p_T^2(J/\psi)$. The differential cross section is plotted. This includes correlated uncertainties.

we find

$$\sigma(p\overline{p} \to J/\psi X, \mid y(J/\psi) \mid < 0.6)$$
$$= 4.08 \pm 0.02(stat)^{+0.36}_{-0.33}(syst)\ \mu\text{b}. \tag{20}$$

To compare with prior measurements where only the portion of the cross section for $p_T(J/\psi)$ exceeding $5\,\text{GeV}/c$ was measured [1], we also measure the integrated cross section of inclusive J/ψ with $p_T > 5\,\text{GeV}/c$ and $|\eta| < 0.6$ at $\sqrt{s} = 1960\,\text{GeV}$. We find the cross section is

$$\sigma(p\overline{p} \to J/\psi X, p_T(J/\psi) > 5.0\ \text{GeV}/c, \mid \eta(J/\psi) \mid < 0.6) \cdot Br(J/\psi \to \mu\mu)$$
$$= 16.3 \pm 0.1(stat)^{+1.4}_{-1.3}(syst)\ \text{nb}. \tag{21}$$

We discuss the comparison of this result with earlier data in Section VII.

VI. $H_b \to J/\psi$ FRACTION AND THE b-HADRON CROSS SECTION

In general, the inclusive J/ψ cross section contains contributions from various sources: prompt production of charmonium; decays of excited charmonium states such as $\psi(2S)$, χ_{c1} and χ_{c2}; and decays of b-hadrons. The charmonium states decay immediately. In contrast, b-hadrons have long lifetimes that are on the order of picoseconds. This implies that J/ψ events from the decays of b-hadrons are likely to be displaced from the beamline. We exploit this feature to separate J/ψ contributions from b-hadrons and prompt charmonium in the p_T bins used in the inclusive J/ψ cross section calculation.

To measure the fraction of J/ψ events that are from displaced decay vertices, we use the subset of the J/ψ sample that includes those events for which both muon tracks from the J/ψ satisfy high quality COT-SVX II track requirements. The track extrapolation from the path formed by the trajectory in the COT into the SVX II is described in Section II C 1. The total number of hits expected in the five layers of the SVX II is determined from the number of functioning and powered silicon sensors intersected by the COT muon track. Tracks missing more than one expected hit in the SVX II are rejected. Both tracks are required to have a hit in the innermost layer of the SVX II and a hit in the second layer if the sensor intersected by the COT track is functioning. Corrections for energy loss in the SVX II are applied to the candidate muons based on a GEANT simulation of the material. The two muon tracks are constrained to come from a common space point. The χ^2 probability of this 3-dimensional vertex fit is required to exceed 0.001. We find that 139200 ± 500 events, or about half of the total J/ψ data sample, pass these criteria. While the data sample is reduced by the SVX II requirements, the momentum, angle, and vertex resolutions are substantially improved.

The primary vertex, taken as the beam position in the r-ϕ plane, is assumed as the point where b-hadrons are produced. It is calculated on a run-by-run basis from a data sample taken using the inclusive jet trigger which has negligible contributions from charm and bottom decays so the beamline position can be calculated with no bias from detached decay vertices. The resolution of the primary vertex in the r-ϕ plane is limited by the ~ 30 μm RMS spread in the size of the beam envelope.

A. Measurement of the Fraction of J/ψ Events from b-hadrons

The J/ψ from the decay of $H_b \to J/\psi X$ is likely to be displaced from the primary vertex where b-hadrons are assumed to be produced. The signed projection of the flight distance of J/ψ on its transverse momentum, $L_{\rm xy}$, is a good measurement of the displaced vertex and can be used as a variable to separate J/ψ of the H_b decay products from that of prompt decays. This method works well for events with high J/ψ p_T where the flight direction aligns well with that of the b-hadron. For events with very low J/ψ p_T, the non-negligible amount of J/ψ with large opening angle between its flight direction and that of the b-hadron will impair the separation ability. Monte Carlo simulation shows that a reliable b-fraction can be extracted using this method for events with J/ψ p_T greater than $1.25\,\mathrm{GeV}/c$.

The $L_{\rm xy}$ is calculated as

$$L_{\rm xy}(J/\psi) = \vec{L} \cdot \vec{p}_T(J/\psi)/|p_T(J/\psi)|, \tag{22}$$

where $\vec{L}$ is the vector from the primary vertex to the J/ψ decay vertex in the r-ϕ plane and $\vec{p}_T(J/\psi)$ is the transverse momentum vector. To reduce the dependence on the J/ψ transverse momentum bin size and placement, a new variable x, called pseudo-proper decay time, is used instead of $L_{\rm xy}$,

$$x = L_{\rm xy}(J/\psi) \cdot M(J/\psi)/p_T(J/\psi), \tag{23}$$

where the $M(J/\psi)$ is taken as the known J/ψ mass [22]. A Monte Carlo simulation is needed to model the distribution of $x(J/\psi)$ from b-hadron events. The Monte Carlo templates of the x distributions $\mathcal{X}_{\rm mc}(x, p_T^{{\rm J}/\psi})$ are generated for all J/ψ transverse momentum ranges and are directly convoluted with the value of the x resolution function measured in the data without allowing any of the parameters governing the shape of the Monte Carlo distributions to vary.

1. *The Likelihood Function*

An unbinned maximum likelihood fit is used to extract the b-fraction, f_B, from the data. The J/ψ pseudo-proper decay time x, its error σ, and the mass of the di-muon pair $m_{\mu\mu}$ are the input variables. A simultaneous mass and lifetime fit is performed using a log-likelihood function ($\ln \mathcal{L}$) given by:

$$\ln \mathcal{L} = \sum_{\rm i=1}^{N} \ln \mathcal{F}(x, m_{\mu\mu}), \tag{24}$$

where N is the total number of events in the mass range $2.85 < m_{\mu\mu} < 3.35\,{\rm GeV}/c^2$.

The mass and pseudo-proper decay time distribution is described by the following function,

$$\begin{aligned} \mathcal{F}(x, m_{\mu\mu}) &= f_{\rm Sig} \times \mathcal{F}_{\rm Sig}(x) \times \mathcal{M}_{\rm Sig}(m_{\mu\mu}) \\ &+ (1 - f_{\rm Sig}) \times \mathcal{F}_{\rm Bkg}(x) \times \mathcal{M}_{\rm Bkg}(m_{\mu\mu}), \end{aligned} \tag{25}$$

where $f_{\rm Sig}$ is the fraction of signal J/ψ events in the mass region, $\mathcal{F}_{Sig}$ and $\mathcal{F}_{Bkg}$ are the functional forms describing the J/ψ pseudo-proper decay time distribution for the signal and background events respectively, and $\mathcal{M}_{\rm Sig}$ and $\mathcal{M}_{\rm Bkg}$ are the functional forms describing the invariant mass distributions for the signal and background events respectively. We now describe these components of the likelihood fit in more detail.

The function for modeling the J/ψ pseudo-proper decay time signal distribution consists of two parts, the $H_b \to J/\psi X$ decay and prompt decay functions labeled $\mathcal{F}_B(x)$ and $\mathcal{F}_P(x)$ respectively:

$$\mathcal{F}_{\rm Sig}(x) = \left[f_B \cdot \mathcal{F}_B(x) + (1 - f_B) \cdot \mathcal{F}_P(x)\right], \tag{26}$$

where f_B is the fraction of J/ψ mesons originating in b-hadron decays. We use the x distributions $\mathcal{X}_{\rm mc}$ of accepted events from a Monte Carlo simulation as templates for the x distribution of b-hadron events in data. The generated distributions are convoluted with a resolution function $R(x'-x, s\sigma)$ such that the $H_b \to J/\psi X$ signal shape is given by

$$\mathcal{F}_B(x) = R(x'-x, s\sigma) \otimes \mathcal{X}_{\rm mc}(x'), \tag{27}$$

where s is an overall error scale factor which represents the possible errors in determining the lifetime resolution and $\otimes$ denotes a convolution. Prompt J/ψ mesons are produced at the primary vertex, therefore their observed displacement is described only by the resolution function $\mathcal{F}_P = R(x, s\sigma)$. We find that $R(x'-x, s\sigma)$ is best described by a sum of two Gaussian distributions centered at $x = 0$.

The background requires a more complicated parameterization to obtain a good fit to the data outside the J/ψ signal region. The pseudo-proper decay time background function is composed of four parts: the zero lifetime component, a positive slope exponential function, a negative slope exponential function, and a symmetric exponential function with both positive and negative slopes. The positive slope exponential function is chosen to model the background from other long lived b-hadron events that produce opposite sign muons such as $b \to c\mu^-\bar{\nu}X, c \to \mu^+\nu X$. The zero lifetime component is chosen to be the same shape as the resolution function. The symmetric and negative slope exponential functions are added to parameterize the remaining components of the background pseudo-proper decay time distributions which are from unknown sources. The background exponential tails are also convoluted with the resolution function.

The background functional form is parameterized as follows:

$$\begin{aligned}
\mathcal{F}_{\rm Bkg}(x) = \ & (1 - f_+ - f_- - f_{\rm sym}) R(x, s\sigma) \\
& + \frac{f_+}{\lambda_+} \exp(-\frac{x'}{\lambda_+}) \theta(x') \otimes R(x'-x, s\sigma) \\
& + \frac{f_-}{\lambda_-} \exp(\frac{x'}{\lambda_-}) \theta(-x') \otimes R(x'-x, s\sigma) \\
& + \frac{f_{\rm sym}}{2\lambda_{sym}} \exp(-\frac{x'}{\lambda_{sym}}) \theta(x') \otimes R(x'-x, s\sigma) \\
& + \frac{f_{\rm sym}}{2\lambda_{sym}} \exp(\frac{x'}{\lambda_{sym}}) \theta(-x') \otimes R(x'-x, s\sigma),
\end{aligned} \tag{28}$$

where $f_{\pm,\ \rm sym}$ is the fraction of the background distribution in the positive, negative and symmetric exponential tails respectively, $\lambda_{\pm,\rm sym}$ are the corresponding exponential slopes, and $\theta(x)$ is the step function defined as $\theta(x) = 1$ for $x \geq 0$ and $\theta(x) = 0$ for $x < 0$. It should be kept in mind that the background strongly depends on p_T and $m_{\mu\mu}$, and that the likelihood function incorporates a global fit over the full mass window shown in Fig. 2, including the J/ψ peak and mass sidebands.

The mass resolution used in the likelihood fit is better than that shown in Figs. 3 - 5 because of the addition of SVX II hits to the tracks. For the likelihood fit, the di-muon mass shape $\mathcal{M}_{\mathrm{Sig}}$ is chosen to be simply the sum of two Gaussian distributions. The means of the Gaussian distributions are allowed to float independently:

$$\begin{aligned}\mathcal{M}_{\mathrm{Sig}}(m_{\mu\mu}) &= G_1(m_{\mu\mu} - M, \sigma_M) \\ &+ f_2 \cdot G_2(m_{\mu\mu} - (M + D), r_2\sigma_M). \end{aligned} \tag{29}$$

The mass fit parameters are the mean M of the mass distribution, the width σ_M of the first Gaussian distribution, the fraction f_2 of the second Gaussian distribution, the shift D in the mean of the second Gaussian distribution, and the ratio r_2 of the widths of the two Gaussian distributions. The mass background is modeled using a linear distribution. This fit is adequate for the SVX II constrained di-muon mass. The function used, normalized to unity over the mass range m^{min} to m^{max} is:

$$\begin{aligned}\mathcal{M}_{\mathrm{Bkg}}(m_{\mu\mu}) &= \frac{1}{m_{\mu\mu}^{max} - m_{\mu\mu}^{min}} \\ &+ M_{\mathrm{slope}}(m_{\mu\mu} - \frac{m_{\mu\mu}^{max} + m_{\mu\mu}^{min}}{2}), \end{aligned} \tag{30}$$

where M_{slope} is the slope of the mass background distribution. The only fit parameter is M_{slope}.

2. *The Fits and Systematic Uncertainties*

The fits to the J/ψ pseudo-proper decay time in three sample p_T ranges are shown in Fig. 7. These data correspond to a subset of the data in the mass plots shown in Fig. 2 which satisfy the SVX II tracking requirements. The values of the b-fractions from the fits with statistical and systematic uncertainties for events with J/ψ transverse momenta of $1.25\,\mathrm{GeV}/c$ to $20.0\,\mathrm{GeV}/c$ are listed in Table V, and the distribution is shown in Fig. 8. This measurement of the b-fraction is used in Section VI B, in conjunction with the measurement of the inclusive J/ψ cross section, to calculate the inclusive b-hadron cross section.

The uncertainties on the b-fractions are summarized in Table VI. In the table, percentage errors on the absolute value of b-fraction are listed. Now we discuss the estimation of systematic uncertainties on the b-fraction in detail.

We have performed various tests to assess the accuracy of the likelihood procedure. The fit shapes for signal and background are histogramed into bins and compared to the binned

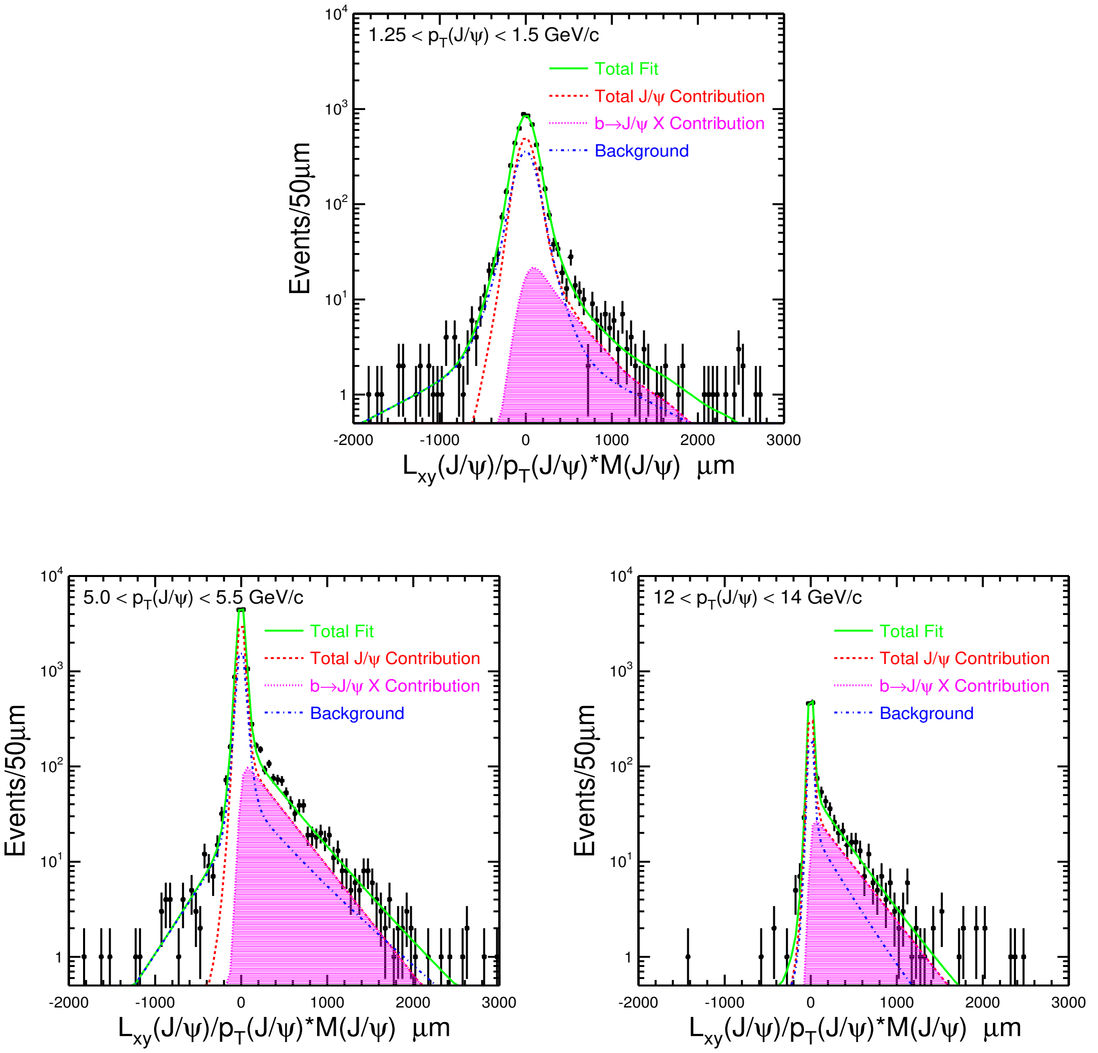

FIG. 7: Fits to the J/ψ pseudo-proper decay time in the ranges of $1.25 < p_T(\mu\mu) < 1.5\,\mathrm{GeV}/c$ (top), $5.0 < p_T(\mu\mu) < 5.5\,\mathrm{GeV}/c$ (bottom left) and $12.0 < p_T(\mu\mu) < 14.0\,\mathrm{GeV}/c$ (bottom right). The solid line is the fit to all the events in the mass window of 2.85 to $3.35\,\mathrm{GeV}/c^2$, the dashed line is the fit to all signal events, the solid histogram is the fit to the portion of the signal events that are from b-hadron decays and the dot-dashed line is the fit to background events including events in the invariant mass sidebands.

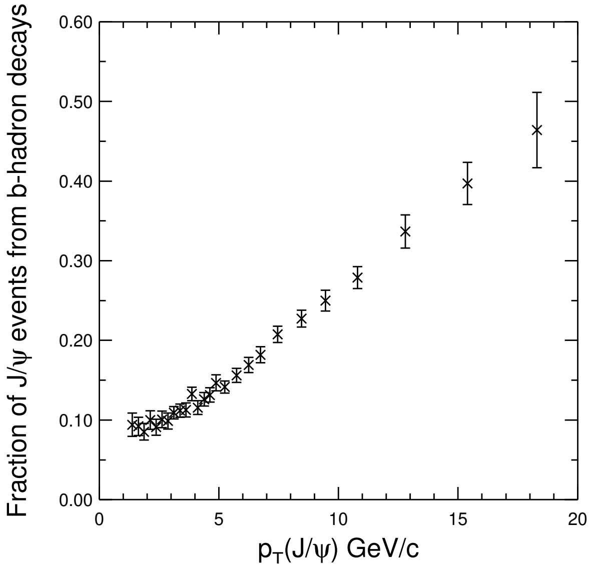

FIG. 8: Fraction of J/ψ from b-hadron decays in the inclusive J/ψ events of Run-II data as a function of J/ψ transverse momentum. Error bars include both statistical and systematic errors.

data distributions. A Kolmogorov-Smirnov (K-S) test [39] is used to compare the fit and data distributions to estimate the quality of the fit. The distribution of K-S probability values for each fit in the different transverse momentum ranges is compared to the K-S probability distributions in a sample of Monte Carlo experiments. The distributions are found to be consistent. In addition to the K-S tests, the normalized residual, defined as the difference between the data and fit projection in units of one standard deviation of statistical error, is compared in every transverse momentum range. Firstly, the data and fit projections are histogrammed using an unequal pseudo-proper decay time bin size so that the number of data events in each bin is more than 20 events to reduce statistical fluctuation. Secondly, the normalized residual distributions are examined. The means and widths of the distributions in all transverse momentum ranges are examined. We find no obvious discrepancies between the fit projection and data distributions.

Monte Carlo samples are also used to determine the potential bias on the b-fraction from the fitting procedure. The pseudo-proper decay time distributions and the invariant mass distributions from signal and background are used to generate a set of 500 statistically independent samples for each of the four p_T bins of 1.25-1.5 GeV/c, 2.0-2.25 GeV/c, 5.0-

TABLE V: The fraction of J/ψ events from decays of b-hadrons and the corresponding acceptance. The first uncertainty on the b-fraction is the statistical uncertainty from the unbinned likelihood fit and the second uncertainty is the combined systematic uncertainties on the measurement of the b-fraction. The uncertainty on the acceptance is the combined statistical uncertainty from Monte Carlo statistics and the systematic uncertainty on the acceptance measurement.

$p_T(J/\psi)$ GeV/c	Fraction from b-hadrons	Acceptance $H_b \to J/\psi X$
$1.25-1.5$	$0.094 \pm 0.010 \pm 0.012$	0.01579 ± 0.00037
$1.5-1.75$	$0.092 \pm 0.006 \pm 0.010$	0.01981 ± 0.00029
$1.75-2.0$	$0.085 \pm 0.006 \pm 0.009$	0.02433 ± 0.00034
$2.0-2.25$	$0.100 \pm 0.005 \pm 0.011$	0.02842 ± 0.00032
$2.25-2.5$	$0.091 \pm 0.005 \pm 0.010$	0.03335 ± 0.00038
$2.5-2.75$	$0.101 \pm 0.005 \pm 0.009$	0.03864 ± 0.00059
$2.75-3.0$	$0.099 \pm 0.005 \pm 0.008$	0.04376 ± 0.00072
$3.0-3.25$	$0.109 \pm 0.005 \pm 0.007$	0.04940 ± 0.00081
$3.25-3.5$	$0.112 \pm 0.005 \pm 0.008$	0.05619 ± 0.00093
$3.5-3.75$	$0.113 \pm 0.005 \pm 0.007$	0.0611 ± 0.0010
$3.75-4.0$	$0.133 \pm 0.005 \pm 0.007$	0.0666 ± 0.0016
$4.0-4.25$	$0.116 \pm 0.005 \pm 0.007$	0.0736 ± 0.0018
$4.25-4.5$	$0.126 \pm 0.006 \pm 0.007$	0.0815 ± 0.0020
$4.5-4.75$	$0.131 \pm 0.006 \pm 0.007$	0.0891 ± 0.0022
$4.75-5.0$	$0.147 \pm 0.007 \pm 0.008$	0.0960 ± 0.0024
$5.0-5.5$	$0.141 \pm 0.005 \pm 0.006$	0.1065 ± 0.0025
$5.5-6.0$	$0.156 \pm 0.006 \pm 0.007$	0.1198 ± 0.0029
$6.0-6.5$	$0.169 \pm 0.007 \pm 0.007$	0.1330 ± 0.0032
$6.5-7.0$	$0.182 \pm 0.007 \pm 0.008$	0.1476 ± 0.0037
$7.0-8.0$	$0.208 \pm 0.006 \pm 0.009$	0.1647 ± 0.0055
$8.0-9.0$	$0.227 \pm 0.009 \pm 0.007$	0.1813 ± 0.0062
$9.0-10.0$	$0.250 \pm 0.011 \pm 0.008$	0.1893 ± 0.0068
$10.0-12.0$	$0.279 \pm 0.012 \pm 0.008$	0.2022 ± 0.0064
$12.0-14.0$	$0.337 \pm 0.019 \pm 0.009$	0.2247 ± 0.0072
$14.0-17.0$	$0.397 \pm 0.025 \pm 0.009$	0.2462 ± 0.011
$17.0-20.0$	$0.464 \pm 0.045^{+0.017}_{-0.011}$	0.2538 ± 0.0093

5.5 GeV/c and 10.0-12.0 GeV/c. Five different values of the b-fraction, 5% to 13%, are assumed and the number of events in each p_T bin is chosen to match the data. The fitted values of b-fractions are found to agree with the generated values within 2% in all p_T bins. Thus the systematic uncertainties on the b-fraction measurements due to fit bias are found to be less than 2%.

TABLE VI: Sources of systematic uncertainties on the measurement of the b-hadron fraction in inclusive J/ψ decays as percentages of the absolute value. In general, the p_T dependent uncertainties increase with decreasing p_T.

Source	Systematic uncertainty
Resolution function model	$\pm(0.5-8)\%$
Background function model	$\pm(0-2)\%$
Fit bias	$\pm(0-2)\%$
MC production spectrum	$\pm(2-7)\%$
MC decay spectrum	$\pm(0.5-3)\%$
MC inclusive H_b lifetime	$\pm(0.5-4)\%$
Total	$\pm(3-13)\%$

The resolution function for the pseudo-proper decay time, $R(x'-x, s\sigma)$, is modeled by a double Gaussian function where the dominant Gaussian width is allowed to float and is determined by the fit to the data in each $p_T(J/\psi)$ bin. Other parameters in the function are fixed to the values obtained from a binned fit to $L_{\rm xy}/\sigma(L_{\rm xy})$ averaged over all $p_T(J/\psi)$. The double Gaussian resolution function is not an exact description of the resolution function shape but only an approximate parameterization of many different resolution effects. Therefore, to estimate the systematic uncertainty due to the resolution function modeling, the maximum range of values for the ratios of areas and widths of the two Gaussians supported by the data are estimated. We find that the ratios of the second Gaussian to the dominant Gaussian vary from 1.5 to 2.5 in width and 0.05 to 0.15 in area. The systematic uncertainty on the b-fraction from this source is largest in the lowest momentum bin, where the percentage error is as large as 8%, and decreases with increasing $p_T(J/\psi)$.

In the J/ψ pseudo-proper decay time signal region, events are observed in the distribution at long positive and negative lifetimes that are not well described by the double Gaussian description of the resolution function. The source of these long lived "tails" is unknown. To estimate the systematic uncertainty on the long lived tails not modeled by the prompt signal double Gaussian, a box shaped function is added to the prompt J/ψ x signal distribution in the range -2500 to 2500 μm. The height of the box is fixed in the fit using the number of events in the data that are in excess of the fit projection. The b-fraction values returned from the fit with the box function are used to estimate the systematic uncertainty from the tails that are not modeled properly. We find the b-fraction values decrease by about 5% in the lowest momentum bins when the box shape is added to the prompt J/ψ distribution. The excess modeled by the box can also be assigned to the b-hadron signal which causes a systematic increase. The change in the b-fraction decreases in the higher transverse momentum bins.

The fit was repeated with the background shape changed such that only a positive and negative exponential is used with no symmetric exponential. The differences in the b-fractions observed are negligible. The background parameters are extracted from a fit to the sideband data distributions only, where the sidebands are chosen such that no significant contribution is expected from the radiative J/ψ tail. The fit is repeated in each bin with the values of the background parameters fixed to the values obtained from the sideband fit. No significant difference between the value of the parameters extracted is observed. The difference in the b-fraction extracted using the parameters obtained from the sideband fit is taken as a systematic uncertainty. In the lowest and highest momentum bin the percentage difference on b-fraction value extracted is 2-3%. The differences are less than 1% in all other bins.

To study the dependence of the b-fractions on the modeling of the b-hadron spectrum used in the Monte Carlo, a flat distribution in p_T and y of the b production spectrum is used to regenerate the x distributions and the fits were repeated. The differences in the value of the b-fractions extracted from the direct fit to Monte Carlo templates of x produced from an input spectrum that is uniform in $p_T(b)$ and $y(b)$ are examined. The variation in the b-fractions extracted in the range 1.25 to 2.0 GeV/c are the largest, the maximum variation being an increase of 18% in the bin 1.5 to 1.75 GeV/c. The uniform input spectrum is unrealistic, therefore the systematic uncertainty is taken as one-half of the size of the variation observed in the b-fraction when the flat model is used. We assign systematic uncertainties of 7%, 3% and 2% for measurements in the transverse momentum ranges of 1.25-3.0 GeV/c, 3.0-8.0 GeV/c and 8.0-20.0 GeV/c respectively.

In addition, we examine the change in the b-fraction extracted when varying the $H_b \to J/\psi X$ decay momentum spectrum while keeping the H_b production momentum spectrum fixed. Two decay spectrums, $H_b \to J/\psi(\text{direct})X$ and $H_b \to J/\psi(\text{inclusive})X$ [40], are used for this. The percentage difference is found to be 2-4% in the lowest momentum bins and $< 1\%$ for $p_T(J/\psi) > 2.5\,\mathrm{GeV/c}$.

The mix of hadrons and their respective lifetimes is a contributing factor to the shape of the J/ψ pseudo-proper decay time distributions. To assess the systematic uncertainty due to the uncertainty on the b-hadron average lifetime, we vary the average lifetime in the Monte Carlo by 11 μm which is the size of the systematic uncertainty on the average b-hadron lifetime measured at CDF in Run II. We find that the measured b-fraction decreases in all transverse momentum bins when the lifetime is increased. The fractional decrease is 4% in the lowest momentum bin and less than 1% for bins with $p_T(J/\psi) > 12\,\mathrm{GeV}/c$. The variation in the b-fraction observed when the average b-hadron lifetime is varied by ± 11 μm is taken as a systematic uncertainty on the b-fraction measurement. Table VI summarizes the sources of systematic uncertainties on the measurement of the b-hadron fraction as percentages of the absolute values.

B. Measurement of the Inclusive b-hadron Cross Section

Since J/ψ mesons from decays of bottom hadrons have a different average spin alignment than an inclusive sample of J/ψ mesons, we need to apply an acceptance correction to account for this difference. In previous CDF measurements, the effective value of the spin alignment parameter α_{eff} of J/ψ from b-hadron decays was measured to be $\alpha_{\mathrm{eff}}(p_T(J/\psi) > 4.0\ \mathrm{GeV}/c) = -0.09 \pm 0.10$ [5], where α_{eff} is obtained by fitting $\cos\theta_{\mathrm{J}/\psi}$, the angle between the muon direction in the J/ψ rest frame and the J/ψ direction in the lab frame, to the functional form $1 + \alpha_{\mathrm{eff}} \cdot \cos^2\theta_{\mathrm{J}/\psi}$. More recent measurement on the spin alignment was done using $B \to J/\psi X$ events collected at the $\Upsilon(4S)$ resonance. The BaBar experiment measured $\alpha_B = -0.196 \pm 0.044$ for $p^* < 1.1\,\mathrm{GeV}/c$ and $\alpha_B = -0.592 \pm 0.032$ for $p^* > 1.1\,\mathrm{GeV}/c$ [41]. Here the decay angle of the J/ψ is measured in the $\Upsilon(4S)$ rest frame and p^* is the total J/ψ momentum measured in the $\Upsilon(4S)$ rest frame.

We opt to use the more precise result from the BaBar experiment in the acceptance calculations for $H_b \to J/\psi X$ events assuming it is applicable to the CDF environment where b-hadrons are produced in fragmentation with a large momentum range instead of produced at a fixed momentum as in Υ decays [15]. First, Monte Carlo events are generated to have the J/ψ helicity angle distributions in the b-hadron rest frame predicted from α_B

values according to their p^* values. Then, values of the spin alignment parameter $\alpha_{\rm eff}$ for events in each J/ψ p_T bin are obtained from fitting the $\cos\theta_{J/\psi}$ distributions of these Monte Carlo events. The systematic errors on $\alpha_{\rm eff}$ are obtained by varying the input values of α_B in the process according to measurement errors. This process gives a result consistent with previous CDF measurement, albeit with smaller uncertainties. For example, a new and more precise value of $\alpha_{\rm eff} = -0.13 \pm 0.01$ for the J/ψ events with $p_T(J/\psi) > 4.0$ GeV/c is obtained from this process. Finally, the acceptance values, as listed in Table V, are calculated from the Monte Carlo events generated with the derived spin alignment parameters in each J/ψ p_T bin.

The differential b-hadron cross sections are calculated in a similar way as that for the inclusive J/ψ. The J/ψ yields in each p_T bin listed in Table I are multiplied with the b-fractions to obtain the corresponding $H_b \to J/\psi$ yields. The new acceptance values listed in Table V are used while the J/ψ reconstruction efficiencies and luminosity value stay the same. Most of the systematic uncertainties in the inclusive J/ψ cross-section calculation carry over here without change except for those from the J/ψ spin alignment on the acceptance which are estimated using errors on $\alpha_{\rm eff}$. In addition, the uncertainties from the b-fractions are also included in the systematic errors. The J/ψ from b-hadron inclusive cross-section results with statistical and systematic uncertainties are shown in Table VII. The differential cross section with all statistical and systematic errors added is plotted in Fig. 9. A recent QCD theoretical calculation using a fixed order (FO) calculation with resummation of next-to-leading logs (NLL) [42] is overlaid. We discuss further the comparison with theoretical calculations in Section VII.

An integration of the differential b-hadron cross-section results in Table VII gives the total cross section

$$\begin{aligned} \sigma(p\bar{p} \to H_b X, p_T(J/\psi) > 1.25\ \mathrm{GeV}/c, |y(J/\psi)| < 0.6) \\ \cdot Br(H_b \to J/\psi X) \cdot Br(J/\psi \to \mu\mu) \\ = 19.4 \pm 0.3(stat)^{+2.1}_{-1.9}(syst)\ \mathrm{nb}. \end{aligned} \tag{31}$$

The systematic uncertainty quoted includes the fully correlated uncertainty of 6.9% obtained from the inclusive J/ψ cross-section measurement. We correct the integrated cross section

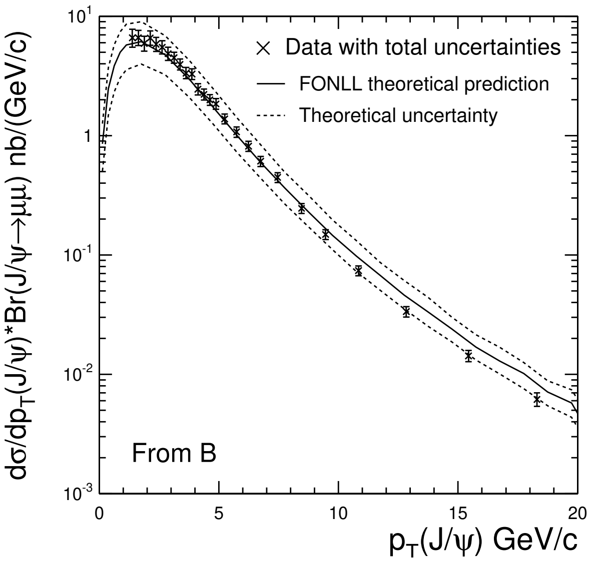

FIG. 9: Differential cross-section distribution of J/ψ events from the decays of b-hadrons as a function of J/ψ transverse momentum integrated over the rapidity range $|y| < 0.6$. The crosses with error bars are the data with systematic and statistical uncertainties added including correlated uncertainties. The solid line is the central theoretical values using the FONLL calculations outlined in [42], the dashed line is the theoretical uncertainty.

extracted above for the branching fraction $Br(J/\psi \to \mu\mu) = 5.88 \pm 0.10\%$ [22] to obtain

$$\begin{aligned} \sigma(p\bar{p} \to H_b,\ H_b \to J/\psi, p_T(J/\psi) > 1.25\ \text{GeV}/c, |y(J/\psi)| < 0.6) \\ = 0.330 \pm 0.005(stat)^{+0.036}_{-0.033}(syst)\ \mu\text{b}. \end{aligned} \tag{32}$$

We also extract the prompt J/ψ cross section by subtracting the cross section of $H_b \to J/\psi X$ from the inclusive J/ψ cross section. This calculation is applied to all J/ψ with $p_T > 1.25\,\text{GeV/c}$ where we are able to extract the b-fraction. The results are shown in Table VII and in Fig. 10. The systematic uncertainties on the prompt J/ψ cross section are taken to be the uncertainties on the inclusive cross section added in quadrature with the uncertainties on the measured b-fractions. We find the integrated cross section of prompt J/ψ to be:

$$\begin{aligned} \sigma(p\bar{p} \to J/\psi_p X, p_T(J/\psi) > 1.25\ \text{GeV}/c, |y(J/\psi)| < 0.6) \\ = 2.86 \pm 0.01(stat)^{+0.34}_{-0.45}(syst)\ \mu\text{b}, \end{aligned} \tag{33}$$

TABLE VII: The inclusive $H_b \to J/\psi X$ and prompt J/ψ differential cross sections as a function of transverse momentum of the J/ψ with statistical and p_T dependent systematic uncertainties. The cross section in each p_T bin is integrated over the rapidity range $|y(J/\psi)| < 0.6$ The fully correlated systematic uncertainty, $syst_{fc} = 6.9\%$, from the measurement of the inclusive J/ψ cross section needs to combined with the p_T dependent systematic uncertainties.

$p_T(J/\psi)$ (GeV/c)	$\langle p_T(J/\psi)\rangle$ (GeV/c)	$\frac{d\sigma}{dp_T} \cdot Br$ (nb/ GeV/c) J/ψ from b	$\frac{d\sigma}{dp_T} \cdot Br$ (nb/ GeV/c) Prompt J/ψ
$1.25 - 1.5$	1.38	$6.60 \pm 0.70(stat)^{+0.77}_{-0.67}(syst_{p_T})$	$66.8 \pm 1.5(stat)^{+9.2}_{-9.1}(syst_{p_T})$
$1.5 - 1.75$	1.63	$6.62 \pm 0.44^{+0.71}_{-0.62}$	$68.6 \pm 1.5^{+8.2}_{-8.0}$
$1.75 - 2.0$	1.87	$5.93 \pm 0.38^{+0.62}_{-0.56}$	$67.0 \pm 1.3^{+7.9}_{-7.7}$
$2.0 - 2.25$	2.13	$6.58 \pm 0.34^{+0.67}_{-0.56}$	$62.5 \pm 0.7^{+7.5}_{-7.4}$
$2.25 - 2.5$	2.38	$5.83 \pm 0.30^{+0.57}_{-0.50}$	$61.5 \pm 0.9^{+7.3}_{-7.2}$
$2.5 - 2.75$	2.62	$5.50 \pm 0.26^{+0.51}_{-0.45}$	$52.1 \pm 0.8 \pm 5.2$
$2.75 - 3.0$	2.87	$4.86 \pm 0.23^{+0.44}_{-0.38}$	$47.1 \pm 0.7 \pm 4.4$
$3.0 - 3.25$	3.12	$4.50 \pm 0.20^{+0.25}_{-0.21}$	$39.1 \pm 0.6 \pm 3.0$
$3.25 - 3.5$	3.38	$3.94 \pm 0.17^{+0.23}_{-0.18}$	$33.4 \pm 0.5 \pm 2.8$
$3.5 - 3.75$	3.62	$3.34 \pm 0.15^{+0.21}_{-0.16}$	$28.2 \pm 0.4 \pm 2.1$
$3.75 - 4.0$	3.87	$3.28 \pm 0.14 \pm 0.16$	$22.9 \pm 0.3 \pm 1.6$
$4.0 - 4.25$	4.12	$2.45 \pm 0.11 \pm 0.15$	$20.1 \pm 0.4 \pm 1.5$
$4.25 - 4.5$	4.38	$2.22 \pm 0.10 \pm 0.11$	$16.5 \pm 0.3 \pm 1.2$
$4.5 - 4.75$	4.62	$1.99 \pm 0.09 \pm 0.10$	$14.1 \pm 0.3 \pm 1.0$
$4.75 - 5.0$	4.88	$1.84 \pm 0.08 \pm 0.10$	$11.5 \pm 0.3 \pm 0.8$
$5.0 - 5.5$	5.24	$1.38 \pm 0.05 \pm 0.06$	$8.92 \pm 0.13 \pm 0.52$
$5.5 - 6.0$	5.74	$1.07 \pm 0.04 \pm 0.05$	$6.21 \pm 0.10 \pm 0.37$
$6.0 - 6.5$	6.24	$0.817 \pm 0.031 \pm 0.038$	$4.29 \pm 0.07 \pm 0.24$
$6.5 - 7.0$	6.74	$0.610 \pm 0.025 \pm 0.026$	$2.93 \pm 0.06 \pm 0.17$
$7.0 - 8.0$	7.45	$0.447 \pm 0.014 \pm 0.022$	$1.82 \pm 0.02 \pm 0.11$
$8.0 - 9.0$	8.46	$0.246 \pm 0.009 \pm 0.010$	$0.894 \pm 0.015 \pm 0.047$
$9.0 - 10.0$	9.46	$0.149 \pm 0.007 \pm 0.006$	$0.473 \pm 0.010 \pm 0.024$
$10.0 - 12.0$	10.8	$0.074 \pm 0.003 \pm 0.003$	$0.204 \pm 0.004 \pm 0.010$
$12.0 - 14.0$	12.8	$0.034 \pm 0.002 \pm 0.001$	$0.069 \pm 0.002 \pm 0.003$
$14.0 - 17.0$	15.4	$0.0143 \pm 0.0009 \pm 0.0007$	$0.023 \pm 0.001 \pm 0.001$
$17.0 - 20.0$	18.3	$0.0062 \pm 0.0006 \pm 0.0004$	$0.0078 \pm 0.0006 \pm 0.0006$

where J/ψ_p denotes a prompt J/ψ and where we have corrected for the $J/\psi \to \mu\mu$ branching fraction.

The differential b-hadron cross section as a function of $p_T(H_b)$ is extracted from the measured differential cross sections of $H_b \to J/\psi X$ by utilizing the decay kinematics of charmonium produced in b-hadron decays.

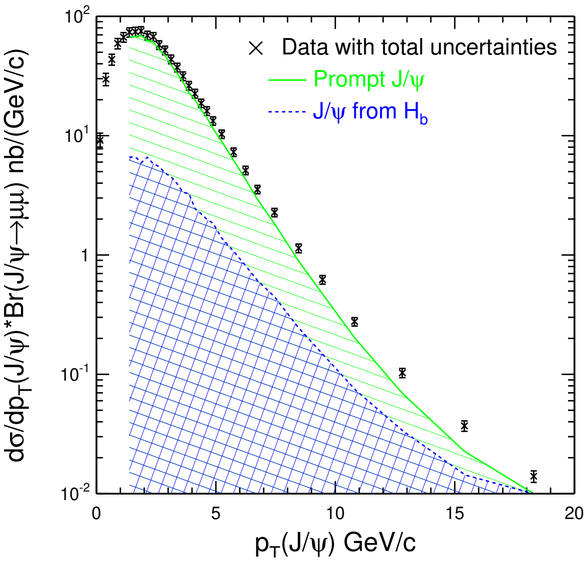

FIG. 10: The inclusive J/ψ cross section as a function of J/ψ p_T integrated over the rapidity range $|y| < 0.6$ is plotted as points with error bars where all uncertainties have been added. The hatched histogram indicates the contribution to the cross section from prompt charmonium production. The cross-hatched histogram is the contribution from decays of b-hadrons.

The procedure starts with the calculation of contributions to the cross section of b-hadrons in a given $p_T(H_b)$ bin from J/ψ events in the range $1.25 < p_T(J/\psi) < 20\,\mathrm{GeV}/c$, where we measured the fractions of J/ψ mesons from b decays. Since b-hadrons with as little as zero momenta produce J/ψ mesons with momenta as large as $2\,\mathrm{GeV}/c$, the measured cross section in this $p_T(J/\psi)$ range is sensitive to the complete $p_T(H_b)$ spectrum. The total contribution to the cross section in the i^{th} bin in $p_T(H_b)$ from events in the accessible $p_T(J/\psi)$ range, labeled as the raw cross section $\sigma_i(raw)$, is given by

$$\sigma_i(raw) = \sum_{\mathrm{j=1}}^{N} w_{ij}\sigma_j(J/\psi), \tag{34}$$

where $\sigma_j(J/\psi)$ is the cross section of J/ψ mesons from H_b in the j^{th} $p_T(J/\psi)$ bin and w_{ij} is the fraction of H_b events in the i^{th} $p_T(H_b)$ bin relative to the total in the j^{th} $p_T(J/\psi)$ bin. The sum of the weights w_{ij} in each $p_T(J/\psi)$ bin is normalized to 1. The raw cross section is corrected for the acceptance due to the limited J/ψ p_T range to obtain the differential

b-hadron cross section, $\sigma_i(H_b)$, in the i^{th} $p_T(H_b)$ bin,

$$\sigma_i(H_b) = \frac{\sigma_i(raw)}{f_\sigma^i} = \frac{\sum_{\mathrm{j=1}}^{N} w_{\mathrm{ij}}\sigma_j(J/\psi)}{f_\sigma^i}, \tag{35}$$

where f_σ^i is the fraction of bottom hadrons in the i^{th} $p_T(H_b)$ bin that give rise to a J/ψ with a transverse momentum in the range 1.25 to 20 GeV/c and rapidity in the range $|y(J/\psi)| < 0.6$. Monte Carlo simulations are used to calculate the weighting factors, w_{ij}, and acceptance correction factors, f_σ^i. In the simulation, the decay spectrum of $H_b \to J/\psi X$ obtained from references [40] and [41] is used. The calculation is repeated in an iteration process: at each pass the input production spectrum used in the Monte Carlo is the spectrum measured in the previous iteration and a χ^2 comparison is made between the input and output spectrums. The process terminates when the χ^2 comparison reaches the precision limit. This procedure is found to be insensitive to the initial production spectrum shape.

The statistical uncertainty in each $p_T(H_b)$ bin is given by:

$$\delta_{\mathrm{stat}}(\sigma_i(H_b)) = \frac{1}{f_\sigma^i}\sqrt{\sum_{j=1}^{N} w_{ij}\delta_{\mathrm{stat}}^2(\sigma_j(J/\psi))}. \tag{36}$$

The systematic uncertainties are taken as just the simple weighted sum of the systematic errors from the differential $H_b \to J/\psi$ cross-sections measurements,

$$\delta_{\mathrm{syst}}(\sigma_i(H_b)) = \frac{1}{f_\sigma^i}\sum_{j=1}^{N} w_{ij}\delta_{\mathrm{syst}}(\sigma_j(J/\psi)). \tag{37}$$

The extracted differential cross section of b-hadrons over the transverse momentum range from 0 to 25 GeV/c is shown in Fig. 11. The cross section has been corrected for the branching fractions, $Br(H_b \to J/\psi X) = 1.16 \pm 0.10\%$ and $Br(J/\psi \to \mu\mu) = 5.88 \pm 0.10\%$ [22], and divided by two to obtain the single b-hadron differential cross section. We integrate the differential cross section extracted above to obtain the single b-hadron inclusive cross section. We find the total inclusive single b-hadron cross section is

$$\sigma(p\bar{p} \to H_b X, |y| < 0.6) = 17.6 \pm 0.4(stat)^{+2.5}_{-2.3}(syst)\ \mu\mathrm{b}. \tag{38}$$

VII. DISCUSSION

We have measured the inclusive J/ψ and b-hadron cross sections in $p\bar{p}$ interactions at $\sqrt{s} = 1960$ GeV in the central rapidity region of $|y| < 0.6$. For the first time, the cross section has been measured over the full transverse momentum range (0-20 GeV/c).

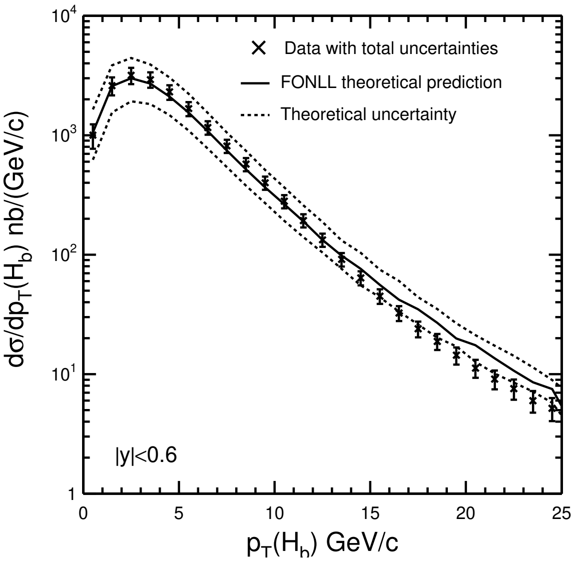

FIG. 11: Differential cross-section distribution of b-hadron production as a function of b-hadron transverse momenta. The crosses with error bars are the data with systematic and statistical uncertainties added, including correlated uncertainties. The solid line is the central theoretical values using the FONLL calculations outlined in [42], the dashed line is the theoretical uncertainty.

For comparison to Run I measurements at $\sqrt{s} = 1800\,\mathrm{GeV}$ [1], we consider the cross-section measurements in the range $p_T(J/\psi) > 5.0\,\mathrm{GeV}/c$ and pseudo-rapidity $|\eta(J/\psi)| < 0.6$. We measure the inclusive J/ψ cross section at $\sqrt{s} = 1960\,\mathrm{GeV}$ to be

$$\sigma(p\overline{p} \to J/\psi X)_{1960} \cdot Br(J/\psi \to \mu\mu) \\ = 16.3 \pm 0.1(stat)^{+1.4}_{-1.3}(syst)\ \mathrm{nb}. \tag{39}$$

The CDF Run I measurement at $\sqrt{s} = 1800\,\mathrm{GeV}$ was found to be

$$\sigma(p\overline{p} \to J/\psi X)_{1800} \cdot Br(J/\psi \to \mu\mu) \\ = 17.4 \pm 0.1(stat)^{+2.6}_{-2.8}(syst)\ \mathrm{nb}. \tag{40}$$

We measure the cross section of J/ψ events from H_b decays with $p_T(J/\psi) > 5\,\mathrm{GeV}/c$ and $|\eta(J/\psi)| < 0.6$ to be

$$\sigma(p\bar{p} \to H_b X)_{1960} \cdot Br(H_b \to J/\psi X) \cdot Br(J/\psi \to \mu\mu) \\ = 2.75 \pm 0.04(stat) \pm 0.20(syst)\ \mathrm{nb}. \tag{41}$$

The equivalent Run I measurement [1] was found to be

$$\sigma(p\bar{p} \to H_b X)_{1800} \cdot Br(H_b \to J/\psi X) \cdot Br(J/\psi \to \mu\mu)$$
$$= 3.23 \pm 0.05(stat)^{+0.28}_{-0.31}(syst) \text{ nb.} \tag{42}$$

Although the Run II J/ψ and b-hadron cross sections are measured at a higher center-of-mass energy, and it is expected that the production cross sections increase by approximately 10%, the Run I and Run II measurements are consistent within measurement uncertainties. The ratio of the Run II to Run I differential b-hadron cross-section measurements as a function of $p_T(J/\psi)$ is shown in Fig. 12. No difference in the shape of the cross section is observed.

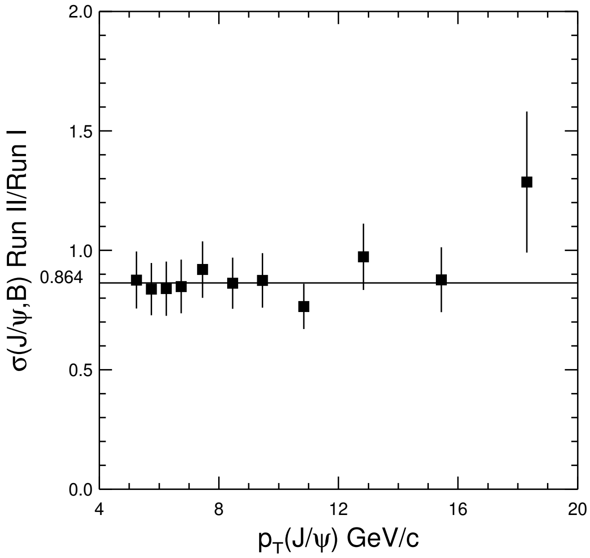

FIG. 12: Ratio of the differential cross-section distributions of J/ψ events from the decays of b-hadrons as a function of J/ψ transverse momentum from CDF Run I and Run II.

In Fig. 13, the B^+ differential cross section previously measured by CDF at $\sqrt{s} = 1800\,\text{GeV}$ for $|y| < 1.0$ [9] is compared with our newer measurement of the inclusive b-hadron differential cross section at $\sqrt{s} = 1960\,\text{GeV}$ extracted from the measurement of the cross section of J/ψ events from b-hadron decays. For the purpose of this comparison, the CDF Run II inclusive b-hadron cross section is multiplied by the fragmentation fraction of B^+ mesons, where the result from LEP experiments is used [43]. In addition, the Run II b-hadron inclusive cross section is scaled up by a factor of 1.67 to extend the measurement to

$|y| < 1.0$ where we have assumed the rapidity distribution is uniform in the region $|y| < 1.0$. As shown in Fig. 13, we find good agreement between the Run II extracted measurement of

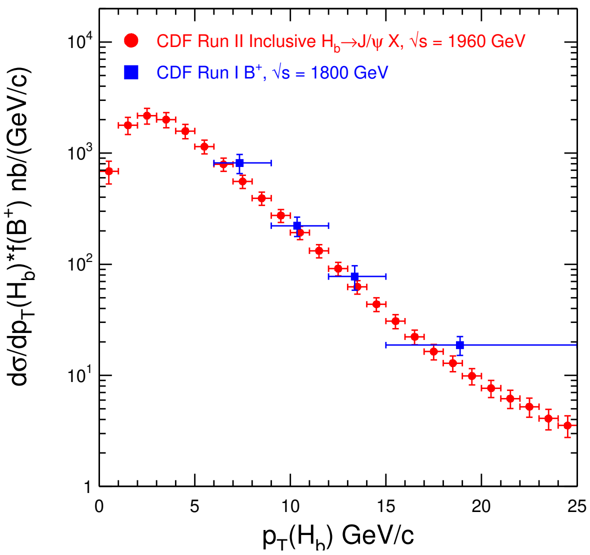

FIG. 13: The differential cross-section distributions of b-hadrons as a function of b-hadron momentum from the measurement of the B^+ meson cross section in CDF Run I [9] and b-hadron inclusive cross section extracted in this analysis (Run II). The differential cross sections showed are integrated over the rapidity range $|y(H_b)| < 1.0$.

the b-hadron cross section and the direct measurement of the B^+ cross section in Run I.

In Fig. 9 and Fig. 11, we compare our measurement to a QCD calculation of the b-hadron cross section by Cacciari *et al.* [42]. This calculation uses a fixed-order approach with a next-to-leading-log resummation and a new technique to extract the b-hadron fragmentation function from LEP data [20, 42]. The single b-hadron cross section from this FONLL calculation using the CTEQ6M parton distribution functions [44] is $\sigma^{FONLL}_{(|\mathrm{y}|<0.6)} = 16.8^{+7.0}_{-5.0}\ \mu$b which is in good agreement with our measurement of $17.6 \pm 0.4(stat)^{+2.5}_{-2.3}(syst)\ \mu$b.

We also compare this result to the QCD calculation described in reference [19]. This calculation employs a factorization scheme where the mass of the quark is considered negligible and a different treatment of the b-hadron fragmentation function is used. The cross-section calculation in [19] is repeated using $\sqrt{s} = 1960\,\mathrm{GeV}/c$ and the MRST2001 parton distribution functions [46]. The central value of the calculated cross section integrated over the rapidity range $|y| < 0.6$ and $p_T(J/\psi) > 5.0\,\mathrm{GeV}/c$ is $\sigma(p\bar{p} \to H_bX, |y| < 0.6) \cdot Br(H_b \to J/\psi X) \cdot Br(J/\psi \to \mu\mu) = 3.2$ nb [45] which is in good agreement with our result of $3.06 \pm 0.04(stat) \pm 0.22(syst)$ nb

A more complete discussion of the changes in QCD calculations can be found in references [18, 20, 42]. Updated determinations of proton parton densities and bottom quark fragmentation functions have brought the QCD calculations into better agreement with the CDF measurements of the total b-hadron cross section and the b-hadron p_T distribution.

VIII. SUMMARY

We have measured the inclusive central J/ψ cross section in $p\bar{p}$ interactions at $\sqrt{s} = 1960\,\mathrm{GeV}$. The cross section has been measured over the full transverse momentum range. for the first time. We find the integrated inclusive J/ψ cross section in the central rapidity range to be

$$\begin{aligned} &\sigma(p\overline{p} \to J/\psi X, \mid y(J/\psi) \mid < 0.6) \\ &= 4.08 \pm 0.02(stat)^{+0.36}_{-0.33}(syst)\ \mu\mathrm{b}, \end{aligned} \tag{43}$$

after correcting for $Br(J/\psi \to \mu\mu) = 5.88 \pm 0.10\%$ [22].

Using the long lifetime of b-hadrons to separate that portion of the J/ψ cross section that is from decays of b-hadrons, we have measured the cross section of J/ψ mesons from b-hadron decays for J/ψ transverse momenta greater than $1.25\,\mathrm{GeV}/c$. The integrated $H_b \to J/\psi X$ cross section, including both hadron and anti-hadron states, is

$$\begin{aligned} &\sigma(p\bar{p} \to H_b,\ H_b \to J/\psi X, p_T(J/\psi) > 1.25\ \mathrm{GeV}/c, |y(J/\psi)| < 0.6) \\ &\qquad = 0.330 \pm 0.005(stat)^{+0.036}_{-0.033}(syst)\ \mu\mathrm{b}, \end{aligned} \tag{44}$$

after correcting for the branching fraction $Br(J/\psi \to \mu\mu) = 5.88 \pm 0.10\%$ [22].

The measurement of the J/ψ cross section from b-hadron decays probes b-hadron transverse momenta down to zero. We have extracted the first measurement of the total central b-hadron cross section in $p\bar{p}$ collisions from the measurement of the b-hadron cross section with J/ψ transverse momenta greater than $1.25\,\mathrm{GeV}/c$ using Monte Carlo models. We find the total single b-hadron cross section integrated over all transverse momenta to be

$$\sigma(p\bar{p} \to H_bX, |y| < 0.6) = 17.6 \pm 0.4(stat)^{+2.5}_{-2.3}(syst)\ \mu\mathrm{b}. \tag{45}$$

Acknowledgments

We thank the Fermilab staff and the technical staffs of the participating institutions for their vital contributions. This work was supported by the U.S. Department of Energy and National Science Foundation; the Italian Istituto Nazionale di Fisica Nucleare; the Ministry of Education, Culture, Sports, Science and Technology of Japan; the Natural Sciences and Engineering Research Council of Canada; the National Science Council of the Republic of China; the Swiss National Science Foundation; the A.P. Sloan Foundation; the Bundesministerium fuer Bildung und Forschung, Germany; the Korean Science and Engineering Foundation and the Korean Research Foundation; the Particle Physics and Astronomy Research Council and the Royal Society, UK; the Russian Foundation for Basic Research; the Commision Interministerial de Ciencia y Tecnologia, Spain; and in part by the European Community's Human Potential Programme under contract HPRN-CT-2002-00292, Probe for New Physics.

---

[1] F. Abe *et al.* (CDF Collaboration), Phys. Rev. Lett. **79**, 572 (1997).
F. Abe *et al.* (CDF Collaboration), Phys. Rev. Lett. **79**, 578 (1997).
T. Daniels, PhD thesis, Massachusetts Institute of Technology, 1997 (unpublished).

[2] G.T. Bodwin, E. Braaten, and G.P. Lepage, Phys. Rev. D **51** 1125 (1995); **55**, 5853(E) (1997).

[3] P. Cho and A. K. Leibovich, Phys. Rev. D **53**, 150 (1996).

[4] A. K. Leibovich, Nucl. Phys. Proc. Suppl. **93** 182 (2001).

[5] T. Affolder *et al.* (CDF Collaboration), Phys. Rev. Lett. **85**, 2886 (2000).

[6] F. Abe *et al.* (CDF Collaboration), Phys. Rev. D **50**, 4252 (1994).

[7] F. Abe *et al.* (CDF Collaboration), Phys. Rev. Lett. **75**, 1451 (1995).

[8] F. Abe *et al.* (CDF Collaboration), Phys. Rev. D **53**, 1051 (1996).

[9] D. Acosta *et al.* (CDF Collaboration), Phys. Rev. D **65**, 052005 (2002).

[10] S. Abachi *et al.* (D0 Collaboration), Phys. Rev. Lett. **74**, 3548 (1995).

[11] B. Abbott *et al.* (D0 Collaboration), Phys. Lett. B **487**, 264 (2000).

[12] B. Abbott *et al.* (D0 Collaboration), Phys. Rev. Lett. **85**, 5068 (2000).

[13] P. Nason, S. Dawson and R. K. Ellis, Nucl. Phys. **B 303**, 607 (1988).

P. Nason, S. Dawson and R. K. Ellis, Nucl. Phys. **B 327**, 49 (1989); **B 335**, 260(E) (1989).

[14] W. Beenakker *et al.*, Nucl. Phys. **B 351**, 507 (1991).

[15] V. Krey and K. R. S. Balaji, Phys. Rev. D **67**, 054011 (2003).

[16] C. Albajar *et al.* (UA1 Collaboration), Z. Phys. C **61**, 41 (1994).

[17] H. Jung, Phys. Rev. D **65**, 034015 (2002).

[18] J. Binnewies, B. A. Kniehl, and G. Kramer, Phys. Rev. D **58**, 034016 (1998).

[19] B. A. Kniehl, and G. Kramer, Phys. Rev. D **60**, 014006 (1999).

[20] M. Cacciari and P. Nason, Phys. Rev. Lett. **89** 122003 (2002).

[21] E. L. Berger, B. W. Harris, D. E. Kaplan, Z. Sullivan, T. M. Tait and C. E. Wagner, Phys. Rev. Lett. **86**, 4231 (2001).

[22] S. Eidelman *et al.*, Phys. Lett. **B 592**, 1 (2004).

[23] F. Abe *et al.*, Nucl. Inst. Meth. A **271**, 387 (1988).

[24] R. Blair *et al.* (CDF Collaboration), FERMILAB-Pub-96/390-E (1996).

[25] A. Sill *et al.*, Nucl. Inst. Meth. A **447**, 1(2000).

[26] T. Affolder *et al.*, Nucl. Inst. Meth. A **526**, 249 (2004).

[27] G. Ascoli *et al.*, Nucl. Inst. Meth. A **268**, 33 (1988).

[28] J. Elias *et al.*, Nucl. Inst. Meth. A **441**, 366 (2000).

[29] D. Acosta *et al.*, Nucl. Inst. Meth. A **461**, 540 (2001).

[30] K. Anikeev *et al.*, IEEE Trans. Nucl. Sci. **47**, 65 (2000).

[31] E.J. Thomson *et al.*, IEEE Trans. Nucl. Sci. **49**, 1063 (2002).

[32] F. Abe *et al.* (CDF Collaboration), Phys. Rev. D **50**, 5550 (1994).

[33] N. Amos *et al.*, Phys. Rev. Lett. **68**, 2433 (1992).

[34] C. Avila *et al.*, Phys. Lett. B **445**, 419 (1999).

[35] M.M. Block and R. N. Cahn, Rev. Mod. Phys **57**, 563(1985).

[36] D. Acosta, *et al.*, Nucl. Inst. Meth. A **494**, 57 (2002).

[37] R. Brun *et al.*, CERN-DD-78-2-REV (unpublished).

[38] P. Avery, K. Read, and G. Trahern, CLEO Report No. CSN-212 1985, (unpublished).

[39] Chakravarti, Laha, and Roy, "Handbook of Method of Applied Statistics", Volume I, John Wiley and Sons, pp. 392-394 (1967).

[40] S. Anderson *et al.* (CLEO Collaboration), Phys. Rev. Lett. **89**, 282001 (2002).

[41] B. Aubert *et al.* (BaBar Collaboration), Phys. Rev. D **67**, 032002 (2003).

[42] M. Cacciari, S. Frixone, M.L. Mangano, P. Nason and G. Ridolfi, JHEP 0407:033, 2004.

[43] Y. Kwon, Phys. Lett **B592**, 712 (2004).

[44] J. Pumplin, D.R. Stump and W. L. Tung, Phys. Rev. D **65**, 014011 (2002);
D. R. Stump *et al.*, Phys. Rev. D **65**, 014012 (2002);
J. Pumplin *et al.*, Phys. Rev. D **65**, 014013 (2002).

[45] Private communication with Berndt Kniehl.

[46] A. D. Martin, R. G. Roberts, W. J. Stirling and R. S. Thorne, Eur. Phys. J. C **23**, 73 (2002) and arXiv:hep-ph/0308087 (2003).